A PASSIVE SAFETY APPROACH TO EVALUATE SPACECRAFT

RENDEZVOUS MISSION RISK

A Thesis

Submitted to the Faculty

of

Purdue University

by

McClain M. Goggin

In Partial Fulfillment of the

Requirements for the Degree

of

Master of Science in Aeronautics and Astronautics

May 2019

Purdue University

West Lafayette, Indiana

THE PURDUE UNIVERSITY GRADUATE SCHOOL
STATEMENT OF THESIS APPROVAL

Dr. David A. Spencer, Chair

    School of Aeronautics and Astronautics

Dr. Kathleen C. Howell

    School of Aeronautics and Astronautics

Dr. Carolin Frueh

    School of Aeronautics and Astronautics

Approved by:

    Dr. Weinong Chen

        Head of the School Graduate Program

ACKNOWLEDGMENTS

I would like to thank all those who have taught, helped, and supported me through my academic career. I want to thank Professor Spencer for guiding my research and always pushing me to expect higher quality. Thank you for your patience and for helping me to simplify things without sacrificing accuracy. Thank you Professor Frueh for providing assistance and expertise where I needed it most, and Professor Howell for teaching me both the fundamentals and advanced concepts in orbital mechanics.

A huge thank you also goes to Dan Dumbacher who became an incredible mentor. I cannot thank you enough for the opportunities you provided me and the friendship you showed me. Thank you, Peter Schulte, for your mentorship and guidance from LA to Adelaide, and Sylvain Renevey for answering an unending stream of questions.

Thank you, Allison Newell, for your incredible ability to edit papers outside of your expertise, and for your unending support and encouragement for me over the last five years. Thank you, Alex Dukes, Kate Fowee, Jake Stewart, Jack Jordan, and Casey Graves for making Purdue University home. I would also like to thank my parents for their love and support, I could not have gotten where I am without you.

Finally, thank you to all my family and friends who have worked through some long days and longer nights, and shaped me into the person I am today.

TABLE OF CONTENTS

LIST OF TABLES

LIST OF FIGURES

SYMBOLS

Bold	Matrix
$(\bar{\cdot})$	Vector
$(\hat{\cdot})$	Unit vector
$(\tilde{\cdot})$	Estimated vector
$\tilde{P}_c$	Propagated collision probability
$\Delta\bar{v}$	Impulsive maneuver
$\bar{z}$	state observation
P_F	Probability of a fault
$\tilde{P}_c\vert_F$	Probability of a fault resulting in a collision
P_T	Total collision probability
$\bar{r}$	Inertial deputy position vector
$^I\bar{v}$	Deputy inertial velocity
$\bar{r}^C$	Inertial chief position vector
$^I\bar{v}$	Deputy inertial velocity
$\bar{\rho}$	Deputy position in chief rotating frame
$^R\dot{\bar{\rho}}$	Deputy velocity with derivative taken in chief rotating frame
L	Rotation matrix
$\bar{h}$	Orbital angular momentum
$\bar{\rho}^C$	Chief position in deputy rotating frame
$^{R_d}\dot{\bar{\rho}}^C$	Chief velocity with derivative taken in deputy rotating frame
$\bar{\xi}$	Relative state in rotating frame
$\bar{\nu}$	Zero-mean Gaussian observation noise
H	Mapping from deputy rotating frame to deputy observation frame
$\mathbf{\Phi}$	State transition matrix
C	State uncertainty covariance

Q	Process noise covariance
$\bar{y}$	Predicted measurement
S	Covariance pre-fit residual
R	Sensor noise covariance
K	Optimal Kalman Gain

ABBREVIATIONS

LVLH   Local Vertical Local Horizontal

EKF   Extended Kalman Filter

UKF   Unscented Kalman Filter

CW   Clohessy-Wiltshire

AD   Approximate Distributions

OS   Orbiting Sample

SRO   Sample Return Orbiter

CHR   Combined Hardbody Radius

ABSTRACT

Goggin, McClain M. M.S., Purdue University, May 2019. A Passive Safety Approach to Evaluate Spacecraft Rendezvous Mission Risk. Major Professor: Dr. David A. Spencer.

Orbital rendezvous enables spacecraft to perform missions to service satellites, remove space debris, resupply space stations, and return samples from other planets. These missions are often considered high risk due to concerns that the two spacecraft will collide if the maneuvering capability of one spacecraft is compromised by a fault.

In this thesis, a passive safety analysis is used to evaluate the probability that a fault that compromises maneuvering capability results in a collision. For a rendezvous mission, the chosen approach trajectory, state estimation technique, and probability of collision calculation each impact the total collision probability of the mission. This thesis presents a modular framework for evaluating the comparing the probability of collision of rendezvous mission design concepts.

Trade studies were performed using a baseline set of approach trajectories, and a Kalman filter for relative state estimation and state estimate uncertainty. The state covariance matrix following each state update was used to predict the resulting probability of collision if a fault were to occur at that time. These trade studies emphasize that the biggest indicator of rendezvous mission risk is the time spent on a nominal intercept trajectory.

1. INTRODUCTION

Sections of this chapter have been adapted from reference [1].

Orbital rendezvous and proximity operations have been an important means of accomplishing complicated missions in space [2]. During the 1960s and 70s, both the United States and the Soviet Union considered orbital rendezvous a key enabling technology for space exploration [3].The decade following the launch of Sputnik in 1957 saw a huge increase in the level of interest in orbital rendezvous. Six years after the first orbital launch, Apollo astronaut Buzz Aldrin submitted his doctoral thesis to MIT on manned orbital rendezvous [4]. In his thesis, with the exception of two references about general celestial mechanics, every reference was published after 1958. By 1965, the first successful orbital rendezvous occurred during the Gemini VI mission, and the first docking on Gemini VIII followed a year later [3]. Orbital rendezvous enabled humans to get to the moon, assemble and maintain space stations, and repair the Hubble space telescope. While Table A.1 shows that over 27 rendezvous vehicles have flown (+4 awaiting first flight), the table does not show the significant number of rendezvous mission concepts currently being developed. Entities ranging from government agencies and universities, to large corporations and small startups, are developing a myriad of rendezvous mission concepts. These concepts include missions to service satellites, remove orbital debris, perform in-space manufacturing, build and supply space stations, and return material from planets, moons, and asteroids. Despite the increasing importance for space applications, orbital rendezvous remains an activity that is a driving risk for many applications. The rendezvous phase of a mission represents a critical time that introduces a substantial amount of operational complexity. When visiting vehicles arrive at the International Space Station, the rendezvous is overseen by astronauts in orbit, teams at NASA Johnson Space Center, and the mission operations center of the vehicle performing

the rendezvous [5]. Despite numerous precautions to reduce mission risk, several orbital rendezvous failures are documented. In 1997, an unmanned Russian Progress resupply vehicle collided with the Mir space station [6]. That same year, the ETS-VII rendezvous and docking demonstration vehicle experienced multiple anomalies during the final phases of rendezvous [7], and in 2005 DARPA's Demonstration of Autonomous Rendezvous Technology (DART) mission experienced an anomaly that resulted in a collision [8, 9]. These failures still affect perceptions about the risks of rendezvous missions.

As the number of rendezvous missions increases, designers may wish to impose a maximum acceptable probability of uncontrolled collision as a design requirement. Program managers may wish to see how this indicator of mission risk is impacted by design decisions and weigh them against the related cost implications. Engineers will want to design an optimal rendezvous for their specific missions. This thesis provides a framework that can be used to evaluate the probability of collision due to loss of maneuverability during the terminal rendezvous phase of a mission.

1.1 Terminal Rendezvous Zones

Every rendezvous mission will pass through three "Zones of Criticality" [10] as shown in Table 1.1. These zones are useful for managing the type of action that must be taken if a spacecraft experiences a malfunction (fault) during the terminal rendezvous. The first zone is the "Passive Safety Zone". While the rendezvous mission is in this zone, the probability that a spacecraft fault will cause the two spacecraft to collide is negligible, even if maneuverability is lost [11]. The second zone is the "Active Abort Zone". Once the rendezvous vehicle enters the active abort zone, any abort that is triggered by a fault will require a maneuver to prevent a collision. The final zone is the "Unavoidable Intercept Zone". Once the rendezvous mission enters this zone the spacecraft does not have adequate thrust to divert from an impact trajectory.

Table 1.1. Definition of "Zones of Criticality"

Zone 1	Zone 2	Zone 3
Passive Safety	Active Abort	Unavoidable Intercept
No maneuver is required to prevent a collision.	A maneuver can be performed to prevent a collision.	No maneuver can be performed to prevent a collision.

1.2 Combined Hardbody

The transition between the passive safety zone and the active abort zone is defined by the probability that the trajectory following a fault will result in a collision. A trajectory is defined as a collision trajectory if the center of mass of one vehicle intersects with combined "hardbody" of both vehicles. This combined hardbody, as shown in Figure 1.1, is typically represented as a sphere with a radius consisting of the combination of the maximum radial dimension of each spacecraft. Using a sphere with the combined hardbody radius (CHR) allows the probability of collision to be determined without an accurate understanding of the attitude of each spacecraft. This hardbody radius is sometimes increased to further add margin by generating a "keep out sphere". The keep out sphere for the international space station is 200 meters [12] while the maximum radial dimension is 65.5 meters. A fault within this keep-out-sphere is considered unacceptable.
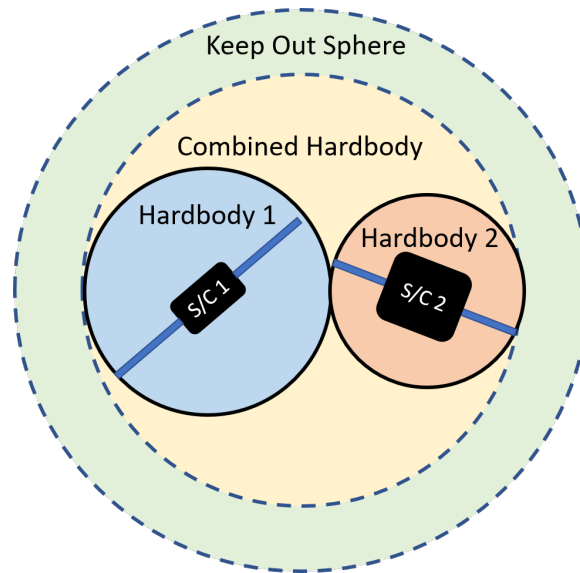
Figure 1.1. Combined hardbody and keep-out-sphere definition for collision determination

1.3 Terminal Rendezvous Key Areas

The probability that a given rendezvous mission design results in a collision is influenced by numerous design decisions including approach trajectory, filter methodology, sensor selection, and hardware reliability. While these design decisions come with other considerations, their impact on mission risk should not be ignored. There are several approaches to calculating the collision probability, and each approach involves a different set of assumptions. Once a method for determining collision probability has been established however, the same method can continue to be used throughout the spacecraft design phase to understand how subsequent design changes alter the collision probability.

1.4 Statement of Purpose

1.4.1 Addressing Stakeholder Issues

This thesis details a framework for estimating the probability of collision for a rendezvous mission while providing a framework that can be updated as design changes are proposed and implemented. The method can enable program managers to weigh the cost of design changes against the corresponding change in collision probability. It can be used by trajectory designers to minimize collision probability based on design parameters, and by fault protection algorithms to determine if the vehicle is in the passive safety or active abort zone.

1.4.2 Determining Rendezvous Collision Probability

The total collision probability for a rendezvous mission is a function of the trajectory design and dynamics models, the state estimation methodology, and the method used to calculate the collision probability. Figure 1.2 shows the flow of information between trajectory design, state estimation, and collision probability determination. The trajectory design provides the relative state $(\rho, \dot{\rho})$ and planned maneuvers $(\Delta \bar{v})$ using the state estimate $(\tilde{\rho}, \dot{\tilde{\rho}})$ determined by the orbit determination filter. The relative position is then observed $(\bar{z})$ using on-board state determination sensors that are simulated by reducing the true relative state to the observable quantities and adding Gaussian white noise. The state estimation filter improves upon these observations and estimates the full state based upon consecutive observations. The state estimate $(\tilde{\rho}, \dot{\tilde{\rho}})$ and state uncertainty covariance $(\mathbf{C})$ are then used to determine the probability that a collision will occur $(\tilde{P}_c)$ if a fault occurs (with a probability of occurring P_F) during the time between observations (t). This probability $(\tilde{P}_c)$ is then used to determine if the spacecraft is in the passive safety or the active abort zone. The total collision probability (P_T) of the terminal rendezvous phase of the mission is then

determined. The total probability of collision for a rendezvous mission can be used to perform trade studies to compare potential mission designs.
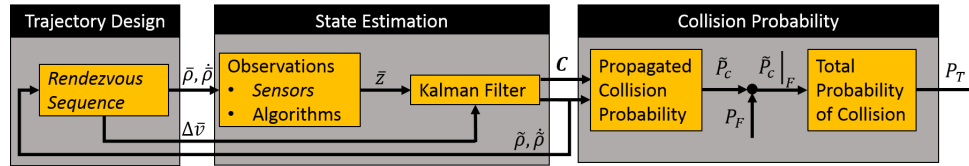
Figure 1.2. Information process flow for rendezvous collision probability

1.5   Scope

While orbital rendezvous can enable many different missions, case studies presented in this thesis investigate the design of a Mars sample return mission involving the capture of an Orbiting Sample canister (OS) by a Sample Return Orbiter (SRO). In this scenario, the one-way light time between Mars and Earth prohibits ground-in-the-loop control of the rendezvous. The absence of GPS and ground-based target tracking around Mars results in the need for an automated rendezvous using the SRO proximity sensor suite for relative state estimation. A rendezvous around Mars is therefore an ideal candidate for a passive safety analysis. In the event of a fault caused by an extended period during which the OS is not visible to the SRO, it would be advantageous for the SRO to be on a low probability of collision trajectory. This trajectory would allow the SRO to passively wait to reacquire visibility of the OS without using additional fuel. The same passively safe trajectory would allow the SRO to completely shut off thrusters in the event of a more serious fault.

Three Mars sample return rendezvous trajectories were used as case studies. These case studies formed the basis of a trade study on the impacts of trajectory changes on the total collision probability. The case studies consisted of a single ballistic trajectory, a straight-line transfer approach, and a two phase approach beginning

with radial impulse transfer "hops" followed by a straight-line transfer along the V-bar as described in Section 1.6.1. Trade studies were then performed to identify how changing trajectory parameters such as the number of "hops" and the location of the transition point between phases affected the total collision probability.

This thesis presents a modular rendezvous collision probability framework. This framework consists of three main areas: a maneuver planning tool, state estimation filter, and collision probability calculator. The scope of each area has been limited to commonly used trajectories, filters, and probability calculations to demonstrate a realistic baseline from which to conduct parameter trade studies. While a fourth area consisting of methods for computer vision and state observation was investigated, implementation of these methods was considered outside of the scope of this thesis due to the significant variation between methodologies. Similarly, control architectures such as artificial potential functions, attitude control schemes, and optimal control laws were considered outside the scope of the current work. However, the developed framework allows new or updated methods in each area, such as control schemes, observation models, and state estimation filters, to be included as part of future work.

1.6 Literature Survey

Extensive research has been conducted in each of the three main areas developed for this thesis. As discussed previously, relative orbital motion and rendezvous trajectories have been heavily investigated since the dawn of the space age. Similarly, one of the first major applications of the Kalman state estimation filter was on the Apollo missions [13].

1.6.1 Rendezvous Dynamics and Approach Trajectories

Relative Motion

The relative motion of interest is that of a "deputy" spacecraft with respect to a non-maneuvering "chief" spacecraft. This motion is commonly described in the local vertical local horizontal (LVLH) reference frame centered on the chief vehicle. This reference frame is alternately known as the RTN, RIC, RSW, and Hill frame [14]. As defined in section 2.1, the LVLH frame consists of the inertial chief radius vector, the inertial chief angular momentum vector, and the vector that completes the right-handed triad in the direction of motion.

Relative Dynamics Models

Extensive work has been done by Scharf et al. [15], Alfriend and Yan [16], and Sullivan et al. [17] to compile the closed form relative dynamics models currently available. These models range from the well-known linear translational model of Hill-Clohessy-Wiltshire (CW) that has seen extensive flight heritage [17] and their extension to curvilinear coordinates by Alfriend et al. [16] and De Bruijn et al. [18], to the orbital element state representation models by Yan [16], and Vallado [19]. The simplest solutions involve the most assumptions such as a circular chief orbit and small spacecraft separation. From these basic models, extensions are made to include either larger spacecraft separations, chief eccentricity [20], perturbations [21, 22], or some combination thereof [23].

Relative geometric formulations developed by D'Amico and Montenbruck [24], as well as those developed by Lovell, Tragesser, and Tollefson [25], with extensions by Lovell and Spencer [26], showed that relative orbital elements can provide geometric insight into the relative motion that is unavailable from other models. This insight can be a significant advantage for preliminary rendezvous design when the assumptions in the underlying dynamics are valid.

Rendezvous Transfers

In Fehse's discussion of rendezvous trajectory types [27], he details ten transfer types for rendezvous with vehicles in near-circular orbits. He groups them into radial impulse transfers, tangential impulse transfers, and straight-line transfers. While radial and tangential impulse transfers take advantage of natural dynamics to make transfer "hops", straight-line transfers use frequent maneuvers to overcome the natural dynamics and travel in a straight line. One common rendezvous approach is to combine a radial impulse transfer and a straight-line transfer with constant velocity. This is a commonly used two-phase approach strategy [2] because the initial portion takes advantage of natural dynamics to introduce some level of passive safety [27] while the final portion overcomes the relative dynamics using thrusters to increases the level of control for a successful docking/mating.

Rendezvous mission sequences typically involve maneuvers, and no maneuver is executed perfectly. Small changes in mass properties and thruster performance over time are very difficult to model, and as such both the magnitude and direction of a maneuver are subject to error. The maneuver error model as presented by Gates [28] was one of the first maneuver execution error models published. This model grouped maneuver errors into proportional and fixed errors for both magnitude and pointing errors. These can be simplified to characterize maneuver error as only proportional magnitude and pointing errors [29].

1.6.2 Relative State Estimation

There are many methods of observing the position of another object. If an object's state is observable, this means that there is sufficient information available to determine that portion of the full state. A single image is sufficient to observe the position of a single point in two dimensions but does not have sufficient information to observe the depth. This is known as an angles only observation. Adding a second camera located a known distance from the first provides stereoscopic vision and can

provide the depth perception in the same way as a pair of eyes. On the other hand, a direct range measurement such as a laser rangefinder can determine the range, but no angles. Sensors such as a LIDAR can observe both the depth and angles, making the full relative position observable. Table 1.2 shows that each of the seven rendezvous mission investigated includes a combination of sensors to make both the range and angles observable.

Table 1.2. Survey of proximity sensors on rendezvous missions

Program/ Project	Narrow Angle	Wide Angle	IR	Video	LIDAR	Laser Range Finder	Inter- Sat link
CPOD	X	X	X				X
Orbital Express	X	X	X	X		X	
PRISMA	X	X					X
ATV			X	X	X	X	
Cygnus			X		X		
Dragon			X		X		
HTV				X		X	

While there are many methods for observing the relative state, all the techniques are susceptible to noise. To produce an improved relative state estimate, the noisy observations are passed through a state estimation filter. One of the important aspects of any state estimation filter is the resulting variance-covariance matrix. This matrix defines a hyper-ellipsoid of the distribution of potential positions and velocities, and an ellipsoid describing the potential positions. This position ellipsoid has a surface with constant probability density [30] and provides a visual representation of where the true relative position is the most likely to be.

The two most common filters used in orbit determination are least squares and sequential processing filters [7]. Least squares filters are ideally suited for quickly obtaining a state estimate from large quantities of data, while sequential processing methods are best suited for improving upon a previous state estimate in real-time while describing the potential error in the state with a covariance matrix. The Kalman filter [31] and its extensions are probably the best known sequential filters and have been extensively used to improve state estimates of dynamic systems from noisy observation data. The Extended Kalman Filter (EKF) is simply the extension of the linear Kalman filter to nonlinear dynamics. As noted by Sullivan [32] the EKF still requires a first order linearization to propagate the state uncertainty covariance.

The Unscented Kalman Filter (UKF) as developed by Julier [33] enables the state uncertainty covariance to be propagated using nonlinear dynamics by generating a representative set of weighted points and propagating them through the nonlinear dynamics. The weights ensure that the state estimate is the mean of the distribution of points both before and after the propagation. The Kalman filter and its extensions are especially suited to the rendezvous problem because they continually update the relative state and covariance as new relative observations are taken.

1.6.3   Collision Probability

There are two broad categories for determining collision probability. The first is through covariance analysis and is the focus of this research. The second is through Monte Carlo analysis which is considered more accurate [34] but is also far more time and resource intensive. A Monte Carlo analysis generates a statistically significant number of potential initial states, propagates them individually, and uses the percent of the initial states that result in a collision as the collision probability.

Covariance analysis uses the assumption that the relative state uncertainty follows a Gaussian distribution. The probability that the true state is located at a given location can then be determined by a Gaussian probability density function.

The collision probability at a single instant in time is determined as the probability that the center of mass of the deputy vehicle lies within the volume of a sphere created by adding together the maximum radius of each spacecraft. Any relative states within this "combined hardbody" are considered to have collided. The two biggest limitations in the accuracy of covariance analysis are the assumption of a Gaussian distribution, and the presence of any unmodeled dynamics when propagating the covariance matrix. When the model used to propagate the covariance is accurate, the accuracy of covariance probability analysis increases.

Methods for calculating collision probability from a state covariance depend on the amount of time the spacecraft spend in close proximity to one another. In his book on spacecraft collision probability Chan [35] categorizes spacecraft collision probability methods based on the relative velocity of the spacecraft. For most orbital spacecraft encounters not involving rendezvous, the relative velocity is high and encounters last only a few seconds. These high velocity encounters are typically modeled as rectilinear motion. There are many methods of calculating collision probabilities for the rectilinear case, however none of them can be directly applied to the low velocity case of a rendezvous where the motion of one spacecraft with respect to another does not resemble a straight line.

Phillips [36] compiled an extensive review and comparison of extended encounter collision probability methods. These methods range from the development of an analytic solution that must be re-derived for any given relative orbit geometry from Chan [35], to methods that break the relative trajectory into small increments of near rectilinear motion that can be combined to generate a total probability of collision such as that by Patera [37], McKinley [38], and Alfano [39]. These methods convert reference frames to a constant covariance centered at the origin of the LVLH frame. They then have the combined hardbody change size and shape with time to sweep out a single a volume representing the entire trajectory. This volume then becomes a function of Cartesian coordinates rather than of time and can be integrated as a time-invariant function. The probability of collision is typically very small when evaluated

near the initial condition but grows swept-out trajectory and hardbody near the chief. In the case of a rendezvous where the deputy range is decreasing while the covariance is expanding, the probability of collision is almost entirely contained within a small portion of the swept-out volume. One useful method for approximating this integral, and thereby saving substantial computation time, is by taking the instantaneous collision probability as determined by a single covariance at the time of maximum collision probability. While this approximation has been shown to slightly under predict the cumulative or total collision probability in certain circumstances [40], it provides a straightforward method for comparing the collision probability of one trajectory to that of a different trajectory. This approximation has been used in this thesis.

1.7   Contributions to State of the Art

This thesis advances the state of the art in three ways. The first is by providing a method for determining if the spacecraft is on a passively safe trajectory at any point during the rendezvous. The second is by providing a modular framework by which the total probability of collision of the rendezvous phase of a mission can be evaluated. Finally, a trajectory parameter trade study is performed that demonstrates how the method can be used to design a passively safe trajectory.

This trade study emphasizes that the time spent on a nominal intercept trajectory is the biggest driver of collision probability. The trade study also shows that while a nominal intercept trajectory places the spacecraft in the active abort zone, not all trajectories in the active abort zone are nominal intercept trajectories. Therefore, a trajectory that is in the active abort zone can decrease the total collision probability, provided it sufficiently reduces the time of flight of the subsequent intercept trajectory. Finally, the trade studies show that for the cases evaluated, a straight-line transfer and a two-phase transfer can provide a reduction in collision probability compared to the single ballistic transfer.

2. MATHEMATICAL APPROACH

Sections of this chapter have been adapted from reference [1].

2.1 Reference Frames

In order to determine the total probability of collision of a given rendezvous mission, it is important to first describe the relative motion. The relative motion of one spacecraft with respect to another is commonly described in the local vertical, local horizontal (LVLH) reference frame of non-maneuvering chief vehicle.
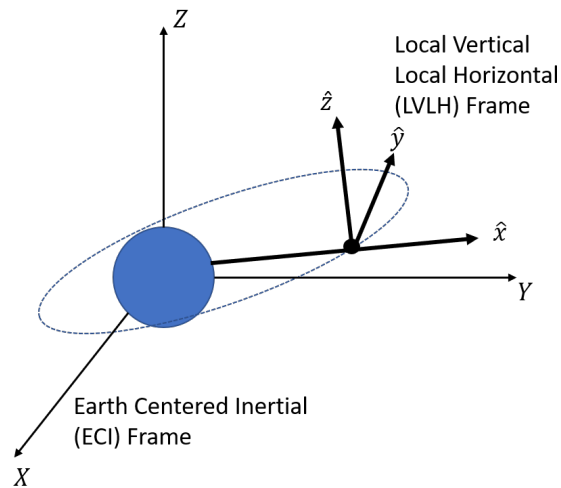
Figure 2.1. Local Vertical, Local Horizontal (LVLH) coordinate system definition for relative orbital motion.

2.1.1 Inertial Reference Frame (I)

The inertial frame (I) for the rendezvous problem is a non-rotating frame centered in the central planetary body with the Z axis pointing in the direction normal to the planet's equator, and the X axis pointing in the direction of the vernal equinox.

2.1.2 LVLH reference frame (R)

The relative motion of a maneuvering deputy vehicle with respect to a non-maneuvering chief vehicle is described in the chief local vertical, local horizontal (LVLH) frame. This frame consists of an $\hat{x}$ component along the chief radius vector, a $\hat{z}$ component along the chief orbital angular momentum vector, and a $\hat{y}$ component that completes the right handed triad as seen in Figure 2.1. For circular chief orbits, the $\hat{y}$ vector lies along the velocity vector. In Figure 2.2,the subscript (C) indicates the LVLH frame centered at the chief.

2.1.3 Body Reference Frame (B)

The final frame of interest is the deputy "body" frame (B). If knowledge of the deputy attitude and inertial state can be assumed, then knowledge of the rotation between the body frame and the LVLH frame can also be assumed. An example of this transformation is provided in Appendix C. All observations provided to the model were assumed to be pre-converted from the body frame to the LVLH frame. This assumption removes the need for an accurate attitude dynamics and control model. Figure 2.2 shows the observation $\bar{z}$ at instant k of the relative state in the body frame subject to Gaussian noise shown by the ellipse surrounding the chief, and the relative position as $\bar{\rho}^C$. Section 2.3.1 describes the mathematical model for simulating an observation.
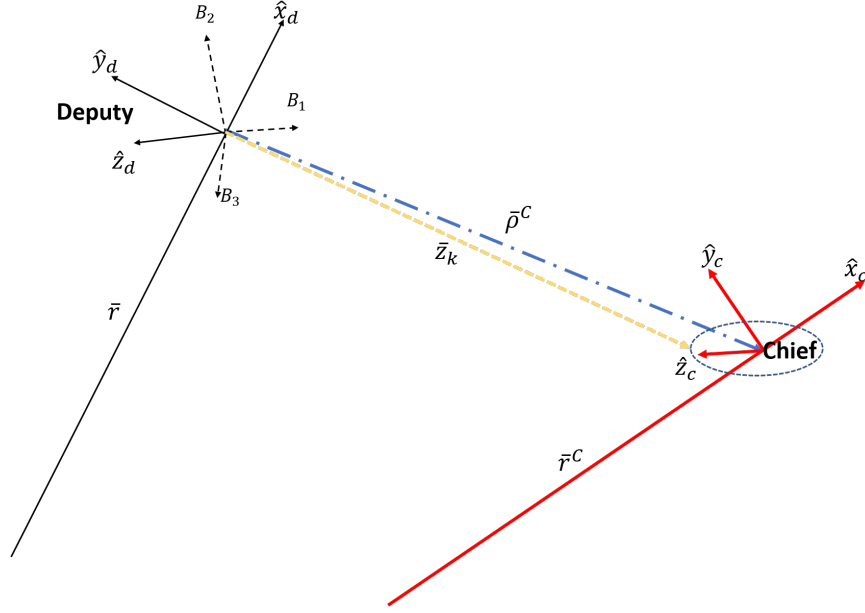
Figure 2.2. Local Vertical, Local Horizontal (LVLH) coordinate system definition for both chief and deputy spacecraft showing deputy body frame, relative position, and observed relative position.

2.1.4 Reference Frame Conversions

To convert the relative state estimate of the chief in the deputy LVLH frame ($\tilde{\xi}^C = [\tilde{\rho}^C, {}^R\dot{\tilde{\rho}}^C]^T$) to the relative state of the deputy in the chief LVLH frame $\tilde{\xi} = [\tilde{\rho}, {}^R\dot{\tilde{\rho}}]^T$, differences in inertial angular velocity must be taken into account.

To obtain the inertial state estimate of the chief from the inertial deputy state and the state estimate of the chief in the deputy LVLH frame, the relative position estimate of the chief ($\tilde{\rho}^C$) is added to the inertial position of the deputy ($\bar{r}$)

$$\tilde{r}^C = \bar{r} + \tilde{\rho}^C \tag{2.1}$$

The inertial deputy velocity $({}^I\bar{v})$ is similarly added to the relative velocity $({}^{R_d}\dot{\tilde{\rho}}^C)$, accounting for the differences in the reference frame in which derivatives were taken.

$${}^I\tilde{v}^C = [{}^I\bar{v} + {}^{R_d}\dot{\tilde{\rho}}^C - (\bar{\Omega} \times \tilde{\rho}^C)] \tag{2.2}$$

where

$$\bar{\Omega} = \bar{h}/||\bar{r}||^2 \tag{2.3}$$

$$\bar{h} = \bar{r} \times {}^I\bar{v} \tag{2.4}$$

To obtain the relative position of the deputy in the chief LVLH frame $(\tilde{\rho})$, the estimated inertial position of the chief $(\tilde{r}^C)$ is subtracted from the deputy position vector:

$$\tilde{\rho} = \bar{r} - \tilde{r}^C \tag{2.5}$$

The relative velocity of the deputy in the chief LVLH frame can be obtained by taking the difference between the inertial velocities and accounting for differences in rotational velocity.

$${}^R\dot{\tilde{\rho}} = {}^I\bar{v} - {}^I\tilde{v}^C - (\tilde{\Omega} \times (\bar{r} - \tilde{r}^C)) \tag{2.6}$$

where

$$\tilde{\Omega} = \tilde{h}/||\tilde{r}^C||^2 \tag{2.7}$$

$$\tilde{h} = \tilde{r}^C \times {}^I\tilde{v}^C \tag{2.8}$$

To plan a maneuver in the inertial frame based on the relative state in the chief LVLH frame, the post-maneuver deputy velocity in the chief LVLH frame $({}^{R_c}\dot{\tilde{\rho}}_f)$ must be converted back to the inertial frame.

$${}^I\tilde{v}_f = [{}^{R_c}\dot{\tilde{\rho}}_f + {}^I\tilde{v}^C - (\tilde{\Omega}^C \times \tilde{\rho})] \tag{2.9}$$

where

$$\tilde{\Omega}^C = \tilde{h}^C/||\tilde{r}^C||^2 \tag{2.10}$$

$$\tilde{h}^C = \tilde{r}^C \times {}^I\tilde{v}^C \tag{2.11}$$

In equations 2.1 to 2.11, the preceding superscript indicates the reference frame in which the derivative is taken, the superscript C following the position or velocity indicates the position or velocity of the chief vehicle while the subscript f indicates the desired state after a maneuver. The $\bar{(\cdot)}$ represents a vector, the $\dot{(\cdot)}$ represents a time derivative, and $\tilde{(\cdot)}$ represents a vector being estimated during the relative orbit determination. The angular momentum is denoted by h, and Ω represents the orbital angular rate. As shown in Figure 2.2, r and v are inertial position and velocities while ρ and $\dot{\rho}$ are relative quantities.

2.2 Dynamics Models

2.2.1 Inertial Dynamics Model

Inertial dynamics were propagated to include the analytical expression for the J_2 spherical harmonic perturbation, as described in Bate's book [41]. The J_2 perturbation was included as the dominant error source rather than separation distance or chief orbit eccentricity, due to the proximity of the spacecraft during terminal rendezvous, and the expectation that the orbiting sample would be placed into a circular parking orbit for retrieval.

$$\ddot{x} + \mu x/d^3[1 + J_2(3/2)(R_m/d)^2(5z^3/d^2 - 1)] = 0 \qquad (2.12)$$

$$\ddot{y} + \mu y \ddot{x}/x = 0 \qquad (2.13)$$

$$\ddot{z} + \mu z/d^3[1 + J_2(3/2)(R_m/d)^3(3 - 5z^2/d^2)] = 0 \qquad (2.14)$$

In 2.12 through 2.14, x, y, z correspond to distances in the inertial X, Y, Z frame, and all derivatives are taken in this frame. The gravitational parameter of the central body is denoted as μ, and J_2 is the spherical harmonic coefficient, R_m is the mean equatorial radius of the central body, and d is the orbital radius of the spacecraft.

2.2.2 Clohessy-Wiltshire Dynamics Model

When the chief orbit is nearly circular, the relative position between the deputy and chief is small, and the relative perturbations are small, the first order approximation of linear relative dynamics described by Clohessy and Wiltshire dominate [42]. In the case of terminal rendezvous with an orbiting sample placed into an equatorial orbit, all of these assumptions are reasonable for small time intervals.

$$\ddot{x} - 2n\dot{y} - 3n^2 x = 0 \tag{2.15}$$

$$\ddot{y} + 2n\dot{x} = 0 \tag{2.16}$$

$$\ddot{z} + n^2 z = 0 \tag{2.17}$$

The analytic solutions can be obtained as derived by reference [42]

$$x(t) = (4x_0 + 2\dot{y}_0/n) - (3x_0 + 2\dot{y}_0/n)\cos\left[n(t - t_0)\right] +$$
$$(\dot{x}_0/n)\sin\left[n(t - t_0)\right] \tag{2.18}$$

$$y(t) = y_0 - 2\dot{x}_0/n - (6nx_0 + 3\dot{y}_0)(t - t_0) +$$
$$(2\dot{x}_0/n)\cos\left[n(t - t_0)\right] + (6x_0 + 4\dot{y}_0/n)\sin\left[n(t - t_0)\right] \tag{2.19}$$

$$z(t) = z_0 \cos\left[n(t - t_0)\right] + (\dot{z}_0/n)\sin\left[n(t - t_0)\right] \tag{2.20}$$

$$\dot{x}(t) = (3nx_0 + 2\dot{y}_0)\sin\left[n(t - t_0)\right] + \dot{x}_0 \cos\left[n(t - t_0)\right] \tag{2.21}$$

$$\dot{y}(t) = -(6nx_0 + 3\dot{y}_0) - 2\dot{x}_0 \sin\left[n(t - t_0)\right] +$$
$$(6nx_0 + 4\dot{y}_0)\cos\left[n(t - t_0)\right] \tag{2.22}$$

$$\dot{z}(t) = -nz_0 \sin\left[n(t - t_0)\right] + \dot{z}_0 \cos\left[n(t - t_0)\right] \tag{2.23}$$

where n is the mean motion of the chief spacecraft, x is the radial distance, y is the along-track distance, and z is the cross-track distance in the chief LVLH frame. All derivatives are taken in the chief LVLH frame.

2.2.3 Relative Orbital Elements

Two major advantages of these linearized equation are the ability to directly solve for relative positions, and the ability to convert them to the more visually intuitive relative orbital elements (ROEs) as presented by Lovell and Tragesser [26]. These ROEs simplify the process of planning rendezvous approaches like the V-bar and straight-line approaches as presented by Fehse. The following equations are reproduced from reference [26].

The radial instantaneous center of motion (x_r) is a function of the LVLH radial position (x_0) and the along-track velocity $(\dot{y}_0)$ and is a constant with respect to time.

$$x_r = 4x_0 + 2\dot{y}_0/n \tag{2.24}$$

The along-track instantaneous center of motion is a function of time, the initial along-track position, and the $\hat{x}$ and $\hat{y}$ velocity.

$$y_r = y_0 - 2\dot{x}_0/n - (6nx_0 + 3\dot{y}_0)(t - t_0) \tag{2.25}$$

The amplitude of the along-track motion, also referred to as the relative semi-major axis, is also a constant with time.

$$a_r = \sqrt{(6x_0 + 4\dot{y}_0/n)^2 + (2\dot{x}_0/n)^2} \tag{2.26}$$

The relative eccentric anomaly describes where along the relative ellipse the spacecraft is located.

$$E_r = \text{atan2}\left(2\dot{x}/n, 6x_0 + 4\dot{y}_0/n\right) + n(t - t_0) \tag{2.27}$$

Finally, the amplitude of the cross-track motion and the cross-track eccentric anomaly are independent of the planar motion and are described entirely by the cross-track position and velocity.

$$A_z = \sqrt{z_0^2 + (\dot{z}_0/n)^2} \tag{2.28}$$

$$\psi = \text{atan2}\left(z_0, \dot{z}_0/n\right) + n(t - t_0) \tag{2.29}$$

In equations 2.24 through 2.29, the x, y, z values are the same is in the CW equations and n is once again the mean motion. As shown in Figure 2.3(a) and 2.3(b), x_r is the radial instantaneous center of relative motion, y_r is the along-track instantaneous center of relative motion, a_r is the amplitude of the along track motion, E_r is the relative eccentric anomaly, A_z is the amplitude of the cross-track motion, and ψ is the cross-track eccentric anomaly.

(a) Relative Geometry: $\hat{x} - \hat{y}$ (b) Relative Geometry: $\hat{x} - \hat{z}$
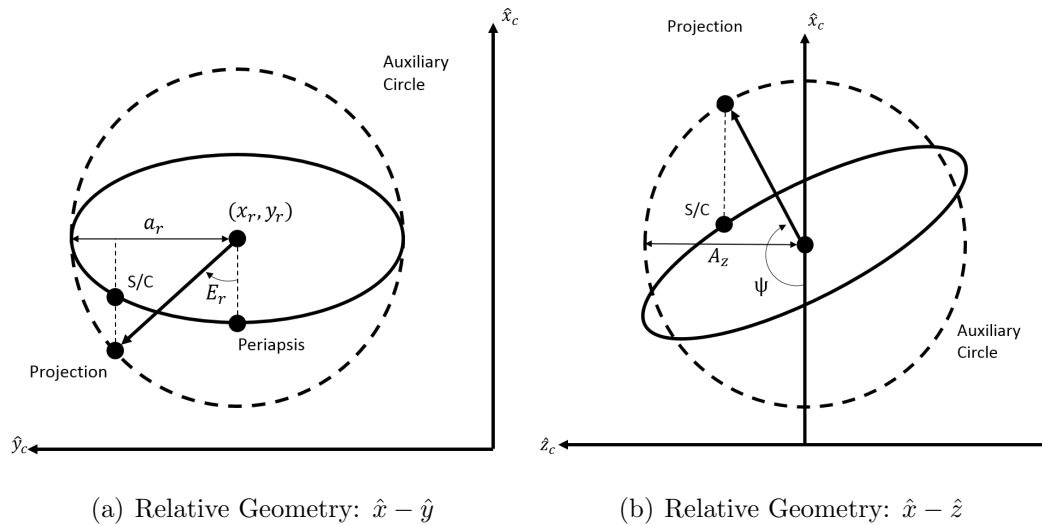
Figure 2.3. Relative orbit geometry as defined by Lovell and Tragesser [25]

A V-bar hop can be visualized as the top (or bottom) portion of the ellipse as shown in Figure 2.3(a). To place the spacecraft on the V-bar hop trajectory the velocity must to match the velocity of the desired ellipse as shown in Figure 2.4(a) Once on the first ellipse, the location of the second maneuver is determined by locating the next crossing of the $\hat{y}_c$ axis, and the $\Delta \bar{v}$ vector is determined by the predicted velocity at the maneuver point and the desired velocity that will place the deputy on an identical trajectory to the first, starting from the now closer position as seen in Figure 2.4(b). If additional passive safety as described by Fehse is desired, the instantaneous center of motion can be moved down in the case of a -V-bar approach, or up in the case of a +V-bar approach in order to force the average motion of the

deputy spacecraft to move away from the chief spacecraft by changing the deputy orbital period.

Maneuvers for a straight-line V-bar approach can be calculated in the same manner by shifting the initial deputy location to the top of the ellipse rather than one side. Maneuvers can be seen in figure 2.5(b).

2.2.4 Relative Motion including J_2 Perturbation

When a more accurate relative state propagation is required, the relative dynamics of Schweighart and Sedwick [21] which include the J_2 perturbation are used.

$$\ddot{x} - 2(nc)\dot{y} - (5c^2 - 2)n^2 x = 0 \tag{2.30}$$

$$\ddot{y} + 2(nc)\dot{x} = 0 \tag{2.31}$$

$$\ddot{z} + (3c^2 - 2)n^2 z = 0 \tag{2.32}$$

where

$$c = \sqrt{1 + s} \tag{2.33}$$

$$s = \frac{3J_2 R_m^2}{8\bar{r}^C}(1 + 3\cos 2i^C) \tag{2.34}$$

In equations 2.30 through 2.34, x, y, z are the relative position of the deputy in the chief LVLH frame, n is the chief mean motion, J_2 is the first zonal harmonic coefficient of the central body, R_m is the mean equatorial radius of the central body, i^C is the reference inclination of the chief vehicle, and c and s are constants.

2.2.5 Maneuver Error

Most rendezvous will consist of one or more maneuvers. Each maneuver is subject to pointing and magnitude errors $\bar{e}_M$ and $\bar{e}_P$. Magnitude errors point along the planned maneuver vector, while pointing errors point in the plane normal to the planned maneuver vector. Maneuver errors are added to the desired error to simulate actual hardware maneuver errors. These errors can be modeled as in reference [29]:

$$\bar{e}_M = E_M||\Delta\bar{v}||\eta\Delta\hat{v} \tag{2.35}$$

$$\bar{e}_P = E_P||\Delta\bar{v}||\hat{\delta} \times \Delta\hat{v} \tag{2.36}$$

where η is a zero-mean Gaussian random variable, $\hat{\delta}$ is a normalized zero-mean Gaussian random vector, and E_M and E_P are the proportional pointing and magnitude errors of the planned maneuver impulse vector $\Delta\bar{v}$, and $\Delta\hat{v}$ is the maneuver unit vector.
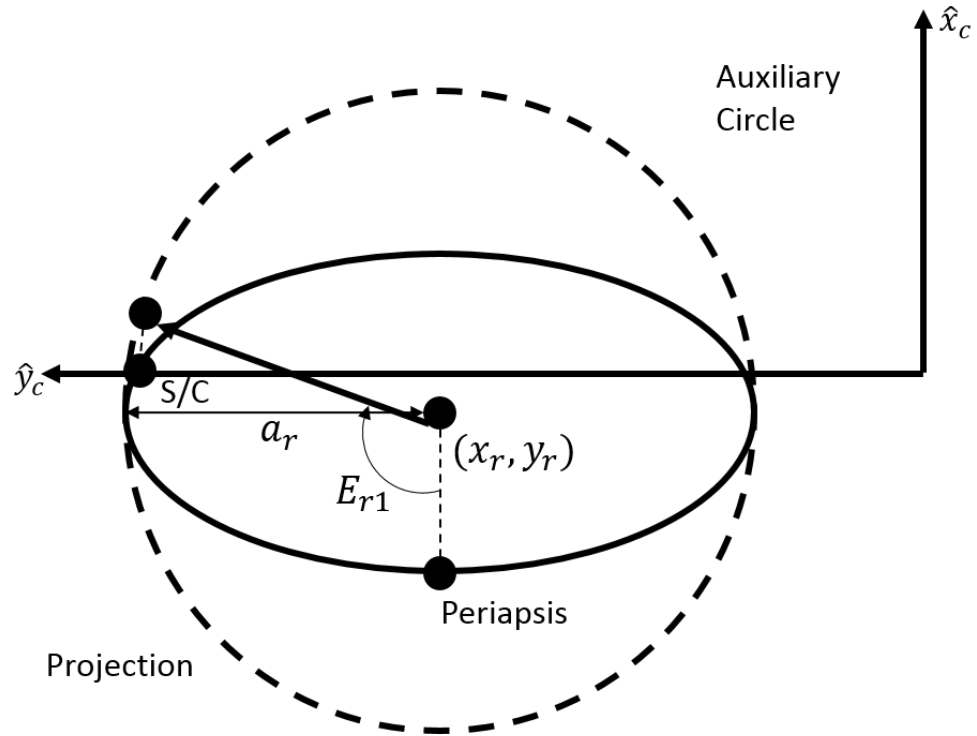
(a) Initial ROE geometry for V-bar hop with spacecraft at the $\hat{y}_c$ axis
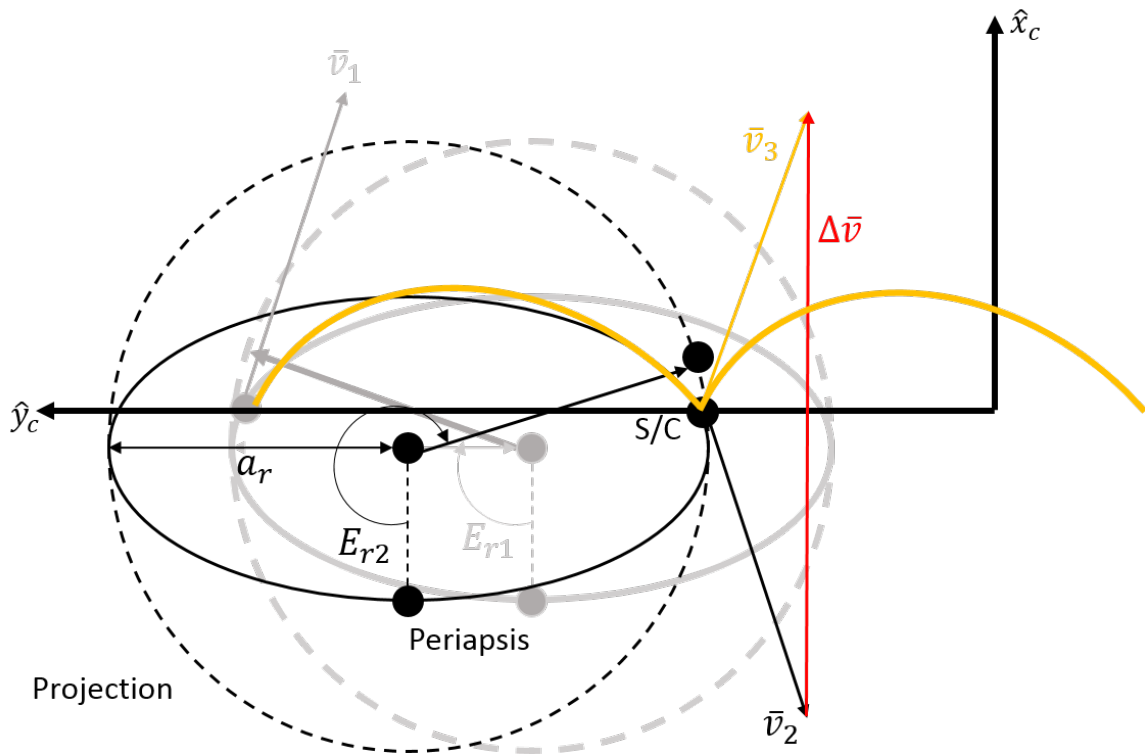
(b) Additional V-bar hop trajectory maneuvers

Figure 2.4. Radial impulse hop maneuver planned using relative orbital elements
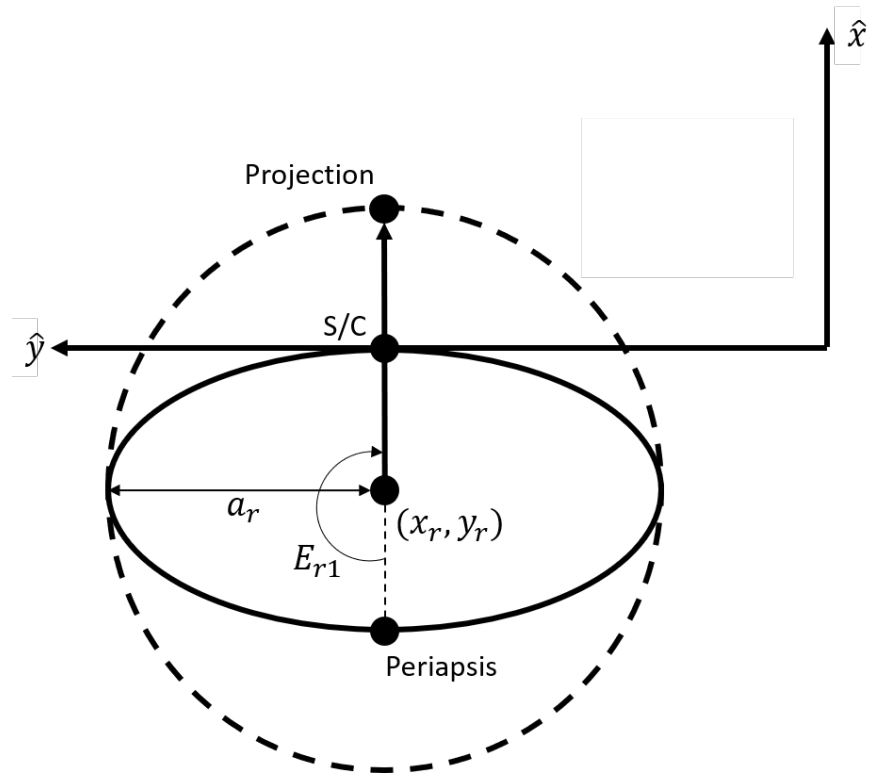
(a) Initial Straight Line Geometry
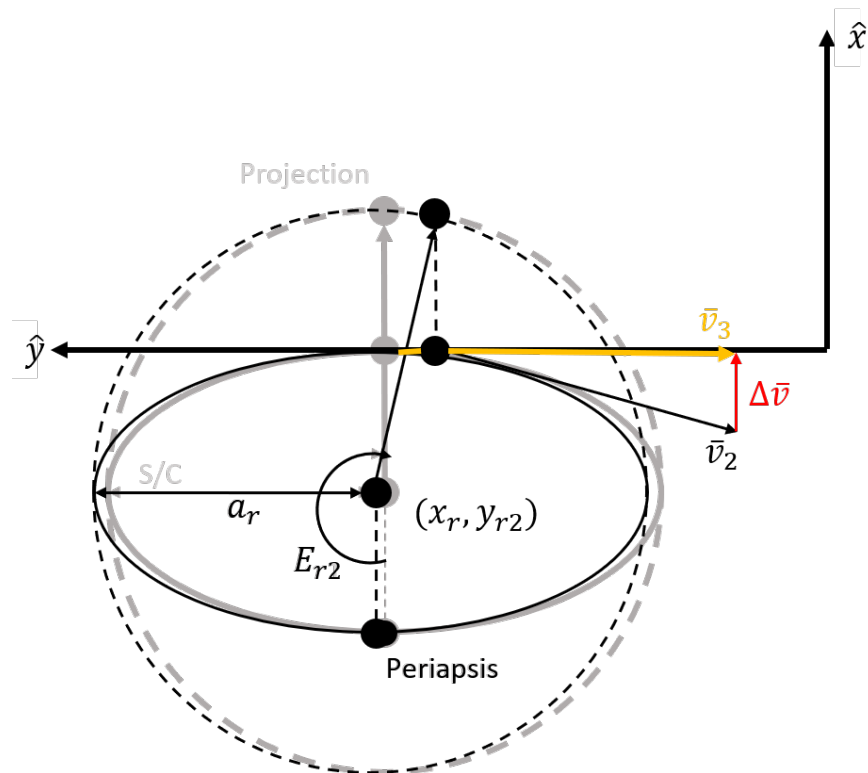
(b) Straight Line Trajectory Maneuvers

Figure 2.5. Straight-line transfer maneuver planned using relative orbital elements

2.3   State Estimation

For the following discussion, the state is assumed to be a 6x1 Cartesian vector consisting of position and velocity, and it is assumed that the relative position is observable such that observations are 3x1 Cartesian vectors.

2.3.1   State Observations

The simplified observation model of the chief state in the deputy LVLH frame is assumed to add Gaussian white noise to the true state as described by Equation 2.38:

$$\bar{\xi}^C = [\bar{\rho}^C, {}^{R_d}\dot{\bar{\rho}}]^T \tag{2.37}$$

$$\bar{z}_k = \mathbf{H}\bar{\xi}^C + \bar{\nu}_k \tag{2.38}$$

Where $\bar{\nu}_k$ is 3x1 a zero-mean Gaussian random variable at observation k, and $\mathbf{H}$ is a 3x6 transformation matrix between the observable states in the body frame and the full state in the deputy LVLH frame. If ${}^B\mathbf{L}^R$ is the 3x3 rotation matrix from the LVLH frame to the Body frame, and if both range and angles are observable, $\mathbf{H}$ is given by

$$\mathbf{H} = [{}^B\mathbf{L}^R, 0_{3x3}] \tag{2.39}$$

where 0_{3x3} is a 3x3 zero matrix. If the deputy is holding its body frame equal to its LVLH frame, ${}^B\mathbf{L}^R$ becomes the 3x3 identity matrix.

2.3.2   The Linear Kalman Filter

In situations where the CW assumptions are valid, a linear Kalman filter can rapidly provide a state estimate and covariance [43]:

Predict

In the prediction step, the previous state estimate and covariance denoted by the subscript $k-1$ is propagated using the 6x6 state transition matrix ($\mathbf{\Phi}$), including any control $\bar{u}$.

$$\tilde{\xi}_{k|k-1} = \mathbf{\Phi}\tilde{\xi}_{k-1} + \mathbf{B}\bar{u}_k \tag{2.40}$$

If $\bar{u}$ is a 3x1 impulse vector, $\mathbf{B}$ is a 6x3 shaping matrix.

$$\mathbf{B} = [0_{3x3}, \mathbf{I}_{3x3}]^T \tag{2.41}$$

The 6x6 covariance $\mathbf{C}$ is then propagated and any unmodeled dynamics are accounted for through the 6x6 process noise matrix $\mathbf{Q}$. Impulsive maneuvers are modeled through an impulsive covariance expansion $\mathbf{C}_{vv}(\bar{u}_k)$, included in appendix D.

$$\mathbf{C}_{k|k-1} = \mathbf{\Phi}\mathbf{C}_{k-1}\mathbf{\Phi}^T + \mathbf{Q} + \mathbf{C}_{vv}(\bar{u}_k) \tag{2.42}$$

Update

The predicted observation ($\bar{y}$) is obtained using the $\mathbf{H}$ matrix

$$\bar{y} = \mathbf{H}\tilde{\xi}_{k|k-1} \tag{2.43}$$

The 3x3 pre-fit residual covariance matrix ($\mathbf{S}$) is then obtained from the expected measurement noise ($\mathbf{R}$) and the predicted covariance ($\mathbf{C}_{k|k-1}$).

$$\mathbf{S} = \mathbf{H}\mathbf{C}_{k|k-1}\mathbf{H}^T + \mathbf{R} \tag{2.44}$$

The 6x3 optimal Kalman gain ($\mathbf{K}$) is determined by the the predicted covariance ($\mathbf{C}_{k|k-1}$) and pre-fit residual covariance matrix ($\mathbf{S}$).

$$\mathbf{K} = \mathbf{C}_{k|k-1}\mathbf{H}^T/\mathbf{S} \tag{2.45}$$

Finally, the updated state estimate is obtained by multiplying the optimal Kalman gain to the pre-fit residual ($\bar{z}_k - \bar{y}$) and adding this to the predicted state estimate.

The updated covariance can then be determined from the predicted covariance and the Kalman gain.

$$\tilde{\xi}_k = \tilde{\xi}_{k|k-1} + \mathbf{K}(\bar{z}_k - \bar{y}) \tag{2.46}$$

$$\mathbf{C}_k = (\mathbf{I} - \mathbf{KH})\mathbf{C}_{k|k-1} \tag{2.47}$$

2.3.3 The Unscented Kalman Filter

When nonlinear dynamics are required, the unscented Kalman filter can provide a more accurate covariance propagation method than an extended Kalman filter. For reference on an extended Kalman filter and the comparison between the two for orbital rendezvous, see reference [17]. The UKF works on the principal that it is easier to approximate a distribution of states than it is to linearize dynamics [33]. The UKF is adapted here from references [44] and [33]:

Predict

A 6x13 matrix $\mathbf{X}$ is first formed, consisting of $2L + 1$ state vectors according to the distribution described by the covariance

$$\lambda = \alpha^2(L + k) - L \tag{2.48}$$

$$\mathbf{X}_0 = \tilde{\xi}_{k-1}^C \tag{2.49}$$

$$\mathbf{X}_i = (\tilde{\xi}_{k-1}^C + \sqrt{(L + \lambda)\mathbf{C}_{k-1}})_i, \{i = 1, ..., L\} \tag{2.50}$$

$$\mathbf{X}_i = (\tilde{\xi}_{k-1}^C - \sqrt{(L + \lambda)\mathbf{C}_{k-1}})_i, \{i = L + 1, ..., 2L\} \tag{2.51}$$

where L is the dimension of the state, λ is a scaling parameter, α determines the spread of the points around the mean $(\tilde{\xi})$ and is typically small, k is a secondary scaling parameter usually set to 0 [44].

These vectors are then numerically propagated according to the nonlinear dynamics models described by Schweighart and Sedwick (SS) [21] to produce a matrix of predicted states ($\mathbf{X}_{k|k-1}$), accounting for any input control ($\mathbf{B}\bar{u}_k$).

$$\mathbf{X}_{k|k-1} = SS(\mathbf{X}_i) + \mathbf{B}\bar{u}_k, \{i = 0, ..., 2L\} \tag{2.52}$$

Weights for the mean and each of the additional state vectors are then formed for both the state estimate (W^m) and covariance (W^c), where β is used to describe the distribution type, $\beta = 2$ is optimal for Gaussian distributions [44].

$$W_0^m = \lambda/(L + \lambda) \tag{2.53}$$

$$W_0^c = \lambda/(L + \lambda) + (1 - \alpha^2 + \beta) \tag{2.54}$$

$$W_i^m = W_i^c = \frac{1}{2(L + \lambda)}, \{i = 1, ..., 2L\} \tag{2.55}$$

The predicted state is approximated using weighted sample mean.

$$\tilde{\xi}_{k|k-1} = \sum_{i=0}^{2L} W_i^m \mathbf{X}_{k|k-1} \tag{2.56}$$

The predicted observation $\bar{y}$ is obtained using a weighted sample mean of the predicted observations of each of the sample points ($\mathbf{Y}$).

$$\mathbf{Y} = \mathbf{H}\mathbf{X}_{k|k-1} \tag{2.57}$$

$$\bar{y} = \sum_{i=0}^{2L} W_i^m \mathbf{Y}_i \tag{2.58}$$

Finally, the predicted covariance of the propagated sample points is determined.

$$\mathbf{C}_{k|k-1} = \sum_{i=0}^{2L} W_i^c [\mathbf{X}_{k|k-1} - \tilde{\xi}_{k|k-1}][\mathbf{X}_{k|k-1,i} - \tilde{\xi}_{k|k-1}]^T \tag{2.59}$$

Update

The pre-fit residual covariance $\mathbf{C}_{\bar{y}_k,\bar{y}_k}$ and the pre-fit residual cross correlation matrix between the mean and the observed states $\mathbf{C}_{\tilde{\xi},\bar{y}_k}$ are formed using the covariance

weights to compute the 6x3 Kalman gain $\mathbf{K}$ incorporating the measurement noise covariance $\mathbf{R}$, assuming that noise is additive and independent

$$\mathbf{C}_{\bar{y}_k,\bar{y}_k} = \mathbf{R} + \sum_{i=0}^{2L} W_i^c [\mathbf{Y}_i - \bar{y}][\mathbf{Y}_i - \bar{y}] \tag{2.60}$$

$$\mathbf{C}_{\tilde{\xi},\bar{y}_k} = \sum_{i=0}^{2L} W_i^c [\mathbf{X}_i - \tilde{\xi}_{k|k-1}][\mathbf{Y}_i - \bar{y}] \tag{2.61}$$

$$\mathbf{K} = \mathbf{C}_{\tilde{\xi},\bar{y}_k} \mathbf{C}_{\bar{y}_k,\bar{y}_k}^{-1} \tag{2.62}$$

The final state estimate and covariance are computed from the Kalman gain and the residual between the expected observation and the actual observation, as in the linear Kalman filter.

$$\tilde{\xi}_k = \tilde{\xi}_{k|k-1} + \mathbf{K}(\bar{z}_k - \bar{y}_k) \tag{2.63}$$

$$\mathbf{C}_k = \mathbf{C}_{k|k-1} - \mathbf{K}\mathbf{C}_{\bar{y}_k,\bar{y}_k}\mathbf{K}^T \tag{2.64}$$

2.4 Collision Probability

2.4.1 Instantaneous Collision Probability

A covariance matrix describes a distribution of points. For a Gaussian distribution, the probability that a point lies within this distribution is determined by a probability density function of the form [45]:

$$P = \frac{1}{\sqrt{2\pi}\sigma} e^{-\frac{1}{2\sigma^2}(x-\mu)^2} \tag{2.65}$$

where σ is the standard deviation, x is the Gaussian random variable, and μ is the mean value.

The probability density function can then be extended to apply to the probability of collision between the three-dimensional state estimate and the volume of the combined hardbody. This instantaneous collision probability is the integrated probability

that the true state lies within the combined hardbody volume. This integration is given by equation 2.66 [35]:

$$P_c(t_j) = \frac{1}{\sqrt{(2\pi)^3 |\mathbf{C_r}|}} \int \int \int_V e^{-.5\bar{d}^T \mathbf{C}^{-1} \bar{d}} dx dy dz \qquad (2.66)$$

where $\mathbf{C_r}$ is the position uncertainty covariance, and $\bar{d}$ is the vector of integration parameters. This vector points from the state estimate to points within the combined hardbody volume.

One method for approximating this integral that does not require numeric integration, is through the method of approximate distributions (AD) as developed by Chan [35]. This approximation typically produces probabilities that agree with numerical integration to a tenth of a percent. The general concept revolves around converting the collision probability integral into a cumulative non-central chi-square distribution (Ψ^2) and then converting to a cumulative central chi-square distribution(χ^2), and finally to the evaluation Gaussian distribution of one variable. If $r = ||\bar{\rho}||$ and the combined hardbody radius is given by R_H, then letting $\chi^2 = X^2$, and $t = T$, when $\Psi^2 = R_H^2$, the probability of collision can be given as the probability:

$$P = P\left[r^2 \leq R_H^2\right] = P\left[\Psi^2 \leq R_H^2\right] = \left[\chi^2 \leq X^2\right] = P\left[t \leq T\right] \qquad (2.67)$$

The method is summarized here, and explained in more depth in Appendix B.

The total mean, variance, and third moment about the mean are given by:

$$\mu = \sum_{j=1}^{3} [\sigma_j^2 + \rho_j^2] \qquad (2.68)$$

$$\mu_2 = 2 \sum_{j=1}^{3} [\sigma_j^4 + 2\sigma_j^2 \rho_j^2] \qquad (2.69)$$

$$\mu_3 = 8 \sum_{j=1}^{3} [\sigma_j^6 + 3\sigma_j^4 \rho_j^2] \qquad (2.70)$$

The degree of the desired central chi-square distribution (χ^2) is given by:

$$n' = \frac{8\mu_2^3}{\mu_3^2} \qquad (2.71)$$

When $\Psi^2 = R^2$, let $\chi^2 = X^2$, giving

$$X^2 = n' + \sqrt{\frac{2n'}{\mu_2}}(R^2 - \mu) \qquad (2.72)$$

Finally, the transformation from a central chi-square distribution to a normal distribution as derived originally by Wilson and Hilferty [46] is given by:

$$T = [\sqrt[3]{\frac{X^2}{n'}} - (1 - \frac{2}{9n'})]/\sqrt{\frac{2}{9n'}} \qquad (2.73)$$

$$P_{MAD} = \frac{1}{2}[1 + erf(T/\sqrt{2})] \qquad (2.74)$$

where ρ_j is the relative position element of the relative position vector $\bar{\rho} = [\rho_1, \rho_2, \rho_3]$, σ is the diagonal element of the position uncertainty covariance (C_r), and R is the combined hardbody radius. The degree of the desired central chi-square distribution(Ψ^2) is given by n', T denotes the desired third moment about the mean, and erf is the error function.

For a spacecraft performing a rendezvous mission, the state uncertainty covariance represents the statistical distribution of possible true states, centered at the state estimate. Equation 2.66 represents the probability that the nominal trajectory intersects the combined hardbody, and therefore the probability that a collision has occurred at that time.

2.4.2 Propagated Collision Probability

A single initial state can be propagated forward in time to determine if it will result in a collision at a later time. Similarly, as is done in Monte Carlo analysis, a distribution of initial states can be propagated forward in time to determine what percent of the original distribution will result in a collision. A state covariance matrix describes the potential distribution of an initial state and can be propagated forward in time to describe what percent of the original distribution will result in a collision. The covariance propagation can be done without requiring the propagation of a statistically significant number of individual initial states.

If a covariance represents the potential distribution of relative states at a given time, sampling this covariance as it is propagated shows the potential distribution of trajectories. The left side of Figure 2.6 shows a planar view in the LVLH frame of a set of three trajectories propagated through 3/4 of an orbit (rev) beginning at 10 meters, 15 meters, and 20 meters from the origin of the LVLH frame. Each figure also shows the corresponding distribution of points as described by the 3σ covariance ellipsoid, sampled at two-minute intervals along the propagated trajectory. The inner arc created by the 3σ ellipsoids shows the potential path of one initial state on the lower boundary of the initial covariance. The outer arc created by the 3σ ellipsoids shows the potential path of a different initial state on the high boundary of the initial covariance. Looking at the intersection of these and other potential trajectories with the combined hardbody radius shows that the time when the most potential trajectories are collision trajectories is represented by a single 3σ covariance ellipsoid. This ellipsoid has been highlighted in red in Figures 2.6(a), 2.6(c), and 2.6(e). Sampling a single collision probability at this location can reduce computation time when compared to other probability estimation methods. This reduction in computation time is important because the relative state estimate and state estimate covariance will have updated initial conditions with every new observation so the probability of collision must also be re-determined with each observation.

The question then becomes how to identify when to calculate the instantaneous collision probability such that it is representative of the likelihood that a collision will occur. For rectilinear motion when relative velocities are high, the location of closest approach is used to calculate the propagated collision probability [35]. For trajectories with low relative velocities this is no longer the case because relatively small variations in trajectories can lead to significantly different locations of maximum collision probability.

The right side of Figure 2.6 shows how the instantaneous collision probability varies along the trajectory shown on the left throughout one full rev. As the trajectory progresses, the state uncertainty grows, and the nominal range from the origin

decreases. For the ten-meter case, the trajectory results in almost 100% of all potential trajectories result in a collision with the combined hardbody. However, every instant along the trajectory does not correspond to a 100% probability of collision. In fact, the point at which the nominal trajectory passes through the origin does not correspond to an instantaneous collision probability of 100%. This can be seen in Figure 2.6(e) where the 3σ state uncertainty covariance has expanded beyond the diameter of hardbody at this point. As the initial trajectory location is changed to 15 and 20 meters, the location in the rev where the maximum collision probability occurs also changes.

To determine the maximum collision probability of a given trajectory, the collision probability throughout the trajectory was determined using the method of approximate distributions (AD) described previously and taking the maximum value.

Figure 2.6(d) shows the instantaneous collision probability as a function of time for the same trajectory as Figure 2.6(c). To emphasize that the minimum range does not correspond to the maximum collision probability, the probability of collision as determined by time of minimum range has been shown. For the specific trajectory shown in figure 2.6(d), the minimum range also produces a good approximation of the maximum collision probability location. However when the same trajectory is initiated at twenty meters as shown in figure 2.6(b) the range no longer produces a good estimate. The maximum collision probability for a propagated trajectory, or "propagated collision probability" ($\tilde{P}_c$), is used to represent the collision probability following an updated state estimate, and can be used to determine if the spacecraft is in the passive safety zone or the active abort zone.
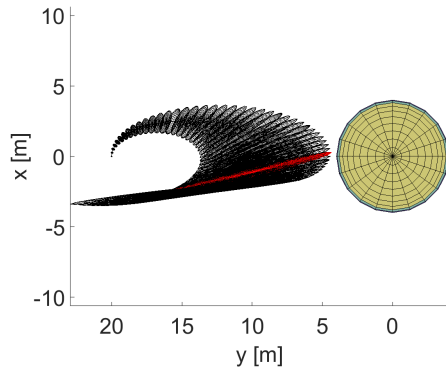
(a) Covariance propagated from 20m
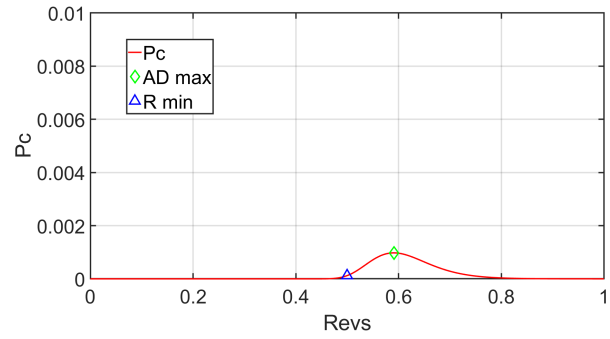
(b) Instantaneous collision probability for 2.6(a)
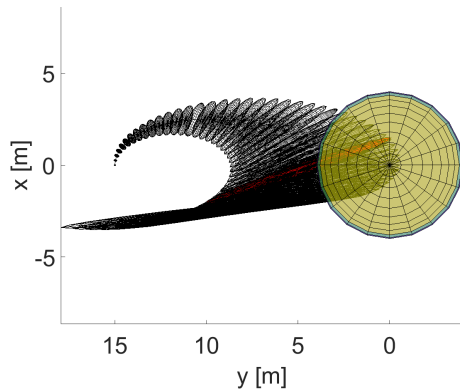
(c) Covariance propagated from 15m
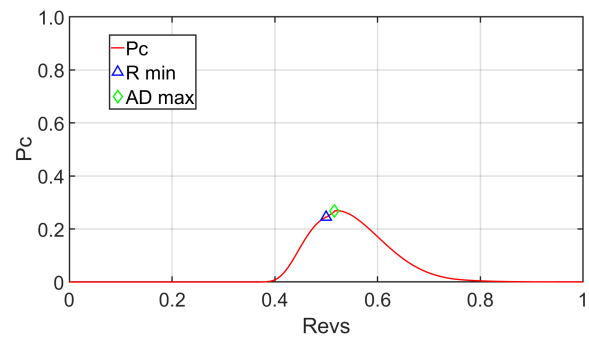
(d) Instantaneous collision probability for 2.6(c)
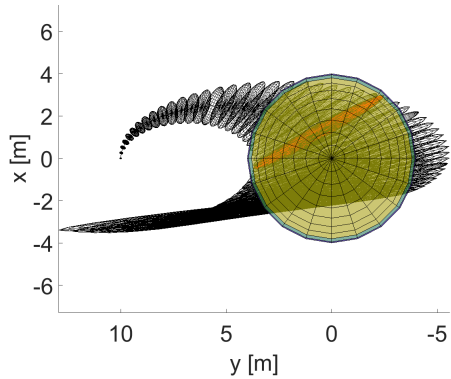
(e) Covariance propagated between 10m and 0m
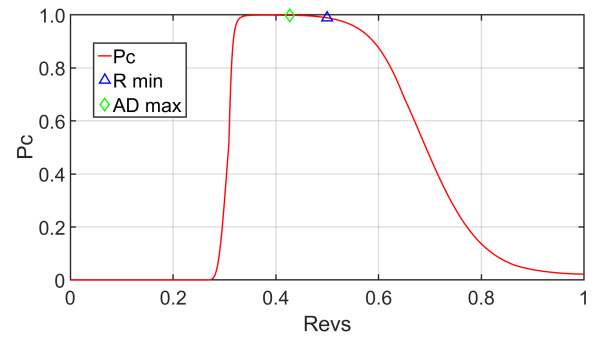
(f) Instantaneous collision probability for 2.6(e)

Figure 2.6. Instantaneous collision probability through 1 rev showing that the point of maximum collision probability corresponds to the instantaneous collision probability described by a single covariance (shown as a red 3σ ellipsoid)

2.4.3 Total Collision Probability

If a fault occurs during the rendezvous sequence, it is assumed that future maneuvers during the approach phase cannot be performed. The probability tree in Figure 2.7 shows a graphical representation of how the total collision probability is calculated.

Figure 2.7 indicates a series of sequential observations, with a node at each time of sensor input. The initial node on the top left indicates the vehicle at time t_1, where a sensor input state observation occurs. The probability that a fault occurs at this time is denoted by P_F. If a fault occurs at t_1, the probability of a collision resulting from the uncontrolled trajectory is equal to the propagated probability of collision from time t_1 ($\tilde{P}_C(t_1)$). The combined probability of impact occurring due to a fault at t_1 is equal to the probability of a fault occurring P_F multiplied with the propagated probability of collision ($P_F\tilde{P}_C(t_1)$).

This combined probability is denoted as $\tilde{P}_c(t_1)|_F$. The resulting propagated collision probability due to a fault at time t_j can be calculated by equation 2.75. For the jth observation, the probability that no faults have occurred is one minus the probability that a fault occurred at any previous observation. The probability that a fault did not occur at the first observation is $(1-P_F)$, the probability that a fault did not occur at either the first or second observation is $(1-P_F)(1-P_F) = (1-P_F)^2$. This formula is known as the binomial distribution for Bernoulli trials. The probability that a fault occurs at the jth observation is P_F. Therefore the probability of a fault occurring at the jth observation and that no faults have occurred up through observation $j-1$ is $P_F(1-P_F)^{(j-1)}$.

$$\tilde{P}_c(t_j)|_F = P_F\tilde{P}_c(t_j)(1-P_F)^{(j-1)} \tag{2.75}$$
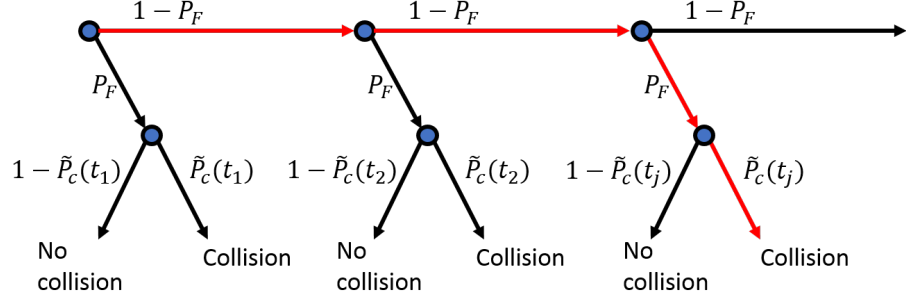
Figure 2.7. Probability tree diagram showing the probability of collision due to an anomaly at any point during the rendezvous sequence

The probability that no collision occurred at each point during the rendezvous sequence $(1 - \tilde{P}_c(t_j))$ can again be determined by a binomial distribution for a Bernoulli trial as seen in Figure 2.8

$$P = \prod_{j=1}^{k} (1 - \tilde{P}_c(t_j)|_F) \tag{2.76}$$

where k is the number of observations between the initialization of the rendezvous sequence and the time of successful capture. This probability includes both the probability of no faults occurring and of no collisions occurring following a fault.
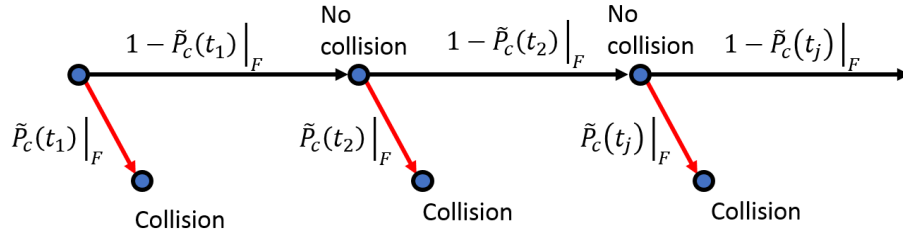

Figure 2.8. Probability tree diagram showing the total probability of no collisions occurring

The probability that a collision occurred at any point during the rendezvous is then one minus the probability that no collisions occurred.

$$P_T = 1 - \prod_{j=1}^{k} (1 - \tilde{P}_c(t_j)|_F) \tag{2.77}$$

3. SIMULATION

3.1 High-Fidelity and Simplified Models

A MATLAB simulation was created to run both a simplified model and a "High-Fidelity" (HIFI) model. The simplified model takes advantage of the linearized CW equations to quickly compare the exact same trajectory while only changing one variable. The HIFI model allows for individual cases to be run in a more realistic manner for detailed study of individual cases and to demonstrate the applicability of this modular framework to fault protection.

3.1.1 Maneuver Planning and Dynamics

The maneuver planner for both the simplified and the HIFI models takes advantages of the geometric representation of ROEs from Lovell and Tragesser. ROEs are used to predict the time at which the maneuvers should occur as well as the planned maneuver vector. Sketches of maneuver planning using ROEs for both V-bar hops and straight line approaches can be seen in figures 2.4(b) and 2.5(b).

For the HIFI mode, the maneuver planner takes in the current state estimate and uses ROEs to predict the time and impulse of the next maneuver. If the time is greater than the deputy observation rate, the nonlinear dynamics of both spacecraft are propagated to the time of the next observation. If the time to the next maneuver is less than the observation rate, the dynamics are propagated to the maneuver time and the impulse including maneuver error is added to the final state. In this way, ROEs are only used to predict the maneuver as far in advance as the time between observations. If a new state estimate informs the maneuver planner that the maneuver should have already occurred, the maneuver is applied a tenth of a second after the

observation. This delay is one the biggest difference between the simplified and high-fidelity models.

For the simplified model, the maneuver planner uses the true state to predict the next maneuver time and propagates to it directly using ROEs. The post maneuver state is then used to determine the subsequent maneuver and post maneuver trajectory. The linear equations of motion allow the entire rendezvous sequence to be created in less than a second with repeatable results. This repeatability allows for one parameter to be changed in a trajectory while leaving all other elements the same for comparison. Both modes plan maneuvers based on a user-input concept of operations matrix consisting of rows describing the type of transfer to be performed and the ending condition. Once the end condition is met, the planner advances to the next phase of the concept of operations.

3.1.2 State Estimation

State estimation is performed in both the simplified model and the high-fidelity mode to minimize the error from the dynamic model used to propagate the true state. In the high-fidelity mode, noisy observations of the true state are passed into the UKF in real time and outputs are provided directly to the maneuver planner. The sensor noise covariance used in the filter is the same as the one used to simulate the observation, representing an accurate understanding of the state observation method and hardware. Process noise on the order of magnitude of the integration tolerance is added to the filter state covariance propagation. Maneuvers are modeled with the planned maneuver and the covariance is expanded impulsively in accordance with the expected maneuver errors.

The simplified model provides the linear Kalman filter with simulated observations from the entire rendezvous. The filter then processes through the observation data adding impulsive covariance expansions corresponding to expected maneuver errors at the maneuver times.

3.1.3   Collision Probability

Once the filter has obtained an updated state and covariance update, the propagated collision probability of the new best estimated trajectory is determined. The state and covariance are propagated using CW approximations at a one second time step for one full rev. The instantaneous collision probability is determined at each timestep, and the maximum collision probability is obtained. This case study only determined the propagated collision probability for one rev beyond the time of a potential fault, because it is assumed that beyond this time, the on-board fault protection system would be able to take sufficient action to either address the fault or actively abort to a predetermined orbit until the issue could be addressed.

In the high-fidelity model, the time of maximum collision probability is used to re-propagate the state and covariance using the unscented transform described in the propagate step of the unscented Kalman filter. This more accurate state and covariance are then used to compute the propagated collision probability using the method of approximate distributions.

Once the last phase of the concept of operations is completed, the total collision probability calculations are performed.

3.2   Capture Conditions

The definition of the "capture condition" or point where the rendezvous ends successfully defines both what trajectories can be evaluated, and where faults stop influencing the collision probability. For example, the fault that occurred on the Gemini VIII mission where a thruster became stuck open after a successful docking, would not be included in a probability of collision analysis, while the same fault occurring less than a meter away just prior to docking would be included. One limitation of using a combined hardbody sphere to model when a collision occurs is that there is likely time between the moment the deputy spacecraft enters this sphere and when an actual successful capture or docking occurs. This simulation assumes

that the boundary of this sphere defines the boundary of the "Unavoidable Intercept Zone" as defined in section 1.1. Cases discussed in the following chapter evaluate both the situation where entering this zone terminates the rendezvous, and where the probability of a fault resulting in a collision is 100% between entering this zone and completing a successful capture at a sphere 1/4 the size of the combined hardbody sphere. This comparison shows how the additional time required to pass through the unavoidable intercept zone can alter what trajectories prove the most effective at reducing the total collision probability.

4. ANALYSIS AND RESULTS

Sections of this chapter have been adapted from reference [1].

4.1 Reference Rendezvous Mission

A motivation for this thesis is the development of a methodology for evaluating the collision probability of a Mars Sample return mission. Table 4.1 Shows the gravitational parameters and assumed reference orbit of the OS.

Table 4.1. Reference mission orbital parameters

Central Body	Mars
Gravitational Parameter	0.042828e15 (m^3/s^2)
Planetary Radius	3396.2 (km)
J_2 Zonal Harmonic Coefficient	1960.45e-6
Altitude	479 (km)
Orbital Period (rev)	2.035 (hours)
Eccentricity	0
Inclination	0 (deg)
Longitude of Ascending Node	0 (deg)
True Anomaly	0 (deg)

4.2 Case Studies

Three cases were chosen as baselines against which to evaluate passive safety. All cases involved a stationary hold at +50 meters along the V-bar $(+\hat{y})$ for 1/2 rev

to allow the filter to converge before maneuvers began. The rendezvous sequence for which the collision probability was estimated began immediately following this hold. Each trajectory ended at the origin of the OS LVLH reference frame, while the calculations of collision probability were terminated after the SRO entered the sphere created by the combined hardbody. The common parameters for both cases can be found in Table 4.2. All results shown for the case studies were computed

Table 4.2. Common rendezvous case parameters

y_0	Initial hold position	50 m
x_r	V-bar hop center of motion	0 m
$\bar{v}_{sl}$	straight line transfer velocity	0.05 m/s
σ_m	Maneuver magnitude error	1.5%
σ_p	Maneuver pointing error	1.5%
P_F	Probability of Fault	1/30 revs
CHR	Combined Hardbody Radius	4 m

using the high-fidelity model, but shown against the simplified or "nominal" model for comparison.

The first case study was a ballistic trajectory initiated from a radial impulse provided in Figure 4.1. The second case studied was that of a straight-line transfer consisting of one initial impulse in the negative V-bar direction of 0.05m/s followed by a trajectory correction maneuver to maintain a straight line every 60 seconds. While this case was called a "straight-line", this maneuver frequency was not sufficient to keep a completely straight line as displayed in Figure 4.3. The third case consisted of a two-phase transfer. The first phase involved four radial impulse transfer hops and ended at ten meters from the origin. The second phase involved a straight-line transfer. The two-phase transfer case can be seen in Figure 4.6.

In addition to these case studies, two primary trajectory trade studies were performed. These trade studies took advantage of the reduced runtime and increased

consistency of the simplified model. The first trade study, shown in Figure 4.9 increased the number of tangential impulse transfer hops used to complete the 50m transfer. The second trade study, shown in Figure 4.10 varied the transition point of the two-phase approach from 40 meters to the origin to determine if a minimum collision probability transition point exists. These trade studies, and the studies performed to further investigate the initial results, emphasize that the most significant factor contributing to the collision probability of a rendezvous mission is the time spent, not distance traveled, on an intercept trajectory.

4.2.1 Ballistic Transfer

Figure 4.1 shows that the trajectory as determined by both the simplified model and the high-fidelity model are consistent. Figure 4.2 shows the propagated probability of collision calculated at each new observation. Within 10 minutes, the filter was able to converge sufficiently to predict a 100 percent probability of collision. This ability to predict that the spacecraft is on a collision trajectory in real time is of significant interest when designing fault protection strategies. Engineers and project sponsors can set collision probability thresholds above which an active abort should be performed, and under which a passive abort should be executed. Figure 4.2 shows that following the initialization of the terminal rendezvous after the initial 1/2 rev hold, the entire rendezvous for the ballistic transfer was clearly in the active abort zone.

Table 4.3 shows a total collision probability of 0.0148 (just under 1/60) based on a probability of a fault occurring once every 30 revs for a 1/2 rev transfer. This The ballistic trajectory only requires one impulse of just over 10.5 mm/s to complete, making it the simplest of the three case studies to execute.

Table 4.3. Ballistic transfer case study results

|	
Total Collision Probability	$0.0149 \pm .00011$
Total Impulse	10.68 mm/s
Number of impulses	1
Elapsed time	0.45 Revs (55 min)
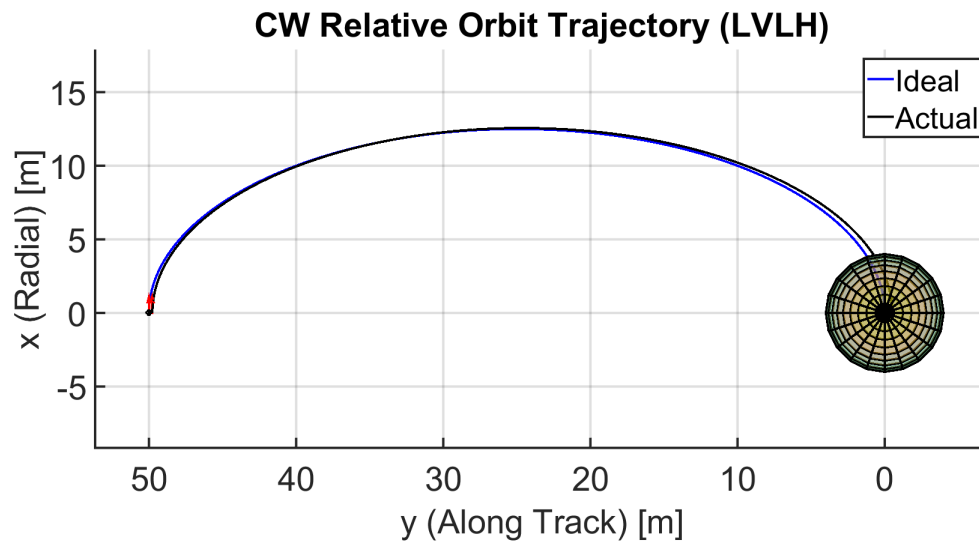
Figure 4.1. Ballistic transfer trajectory from a single radial burn at 50 meters showing simplified and HIFI models
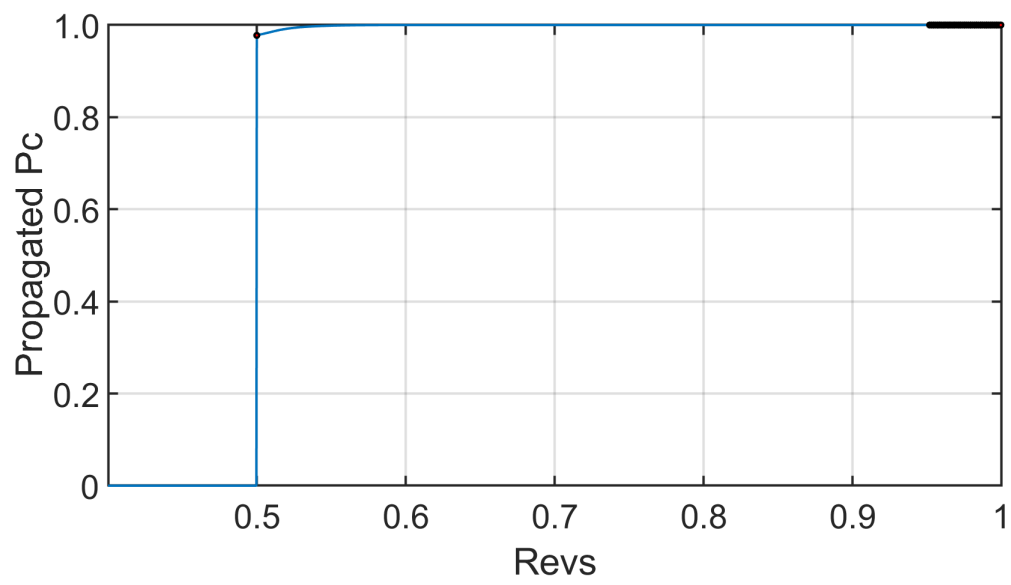
Figure 4.2. Ballistic Transfer propagated collision probability

4.2.2 Straight-Line Transfer

Figure 4.3 shows that both the simplified model and high-fidelity model were unable to maintain an exactly straight line due to the assumed maximum maneuver frequency of 1/60 seconds. This figure shows the difficulty of completely overcoming the relative orbital motion.

Figure 4.4 shows the predicted trajectories that would occur following a fault at the time of a maneuver if the subsequent maneuver were not performed. Figure 4.4 demonstrates that the straight-line trajectory was nominally passively safe until the 13th maneuver that occurred at a range of 14 meters. After this maneuver, the nominal trajectory would have intercepted the combined hardbody even if the maneuver at 11 meters were not performed.

Figure 4.5 shows the propagated collision probability for the straight-line transfer. This shows that not only did the 13th maneuver result in a nominal intercept, but also that this maneuver resulted in a propagated collision probability of 1. This is in contrast to the ballistic trajectory maneuver which was only predicted to have a 0.98 probability of collision immediately following the maneuver. This difference is due to the drastically reduced time between 13th maneuver in the straight-line trajectory and the intercept point, and the time between the ballistic trajectory maneuver and predicted intercept point.

Table 4.4 shows that the total collision probability was reduced by an order of magnitude from the ballistic trajectory case while the number of impulses and total impulse were increased by an order of magnitude.

Table 4.4. Straight-line transfer case study results

|	
Total Collision Probability	$0.0011 \pm .00000$
Total Impulse	146 mm/s
Number of impulses	17
Elapsed time	0.04 revs (4.88 min)
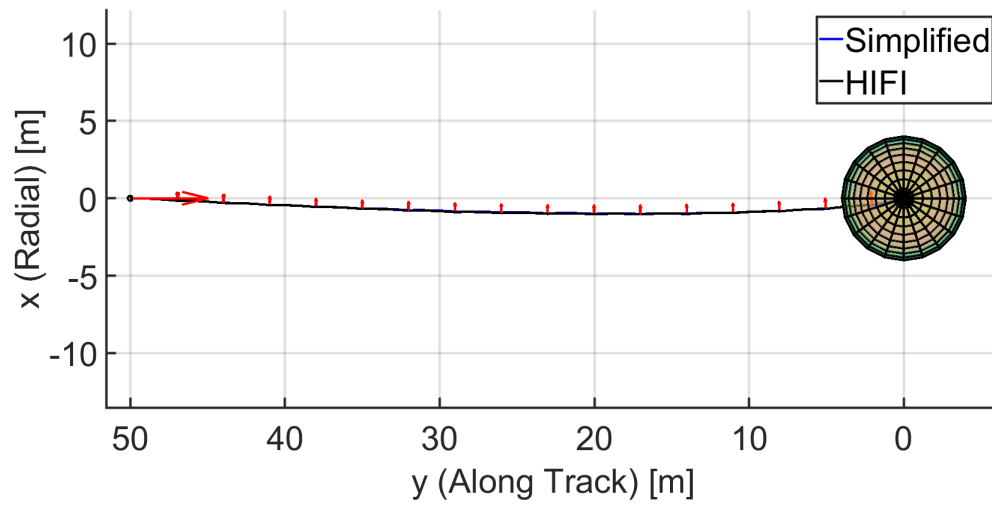
Figure 4.3. Straight-line transfer trajectory from trajectory correction maneuvers at one minute intervals showing simplified and HIFI models
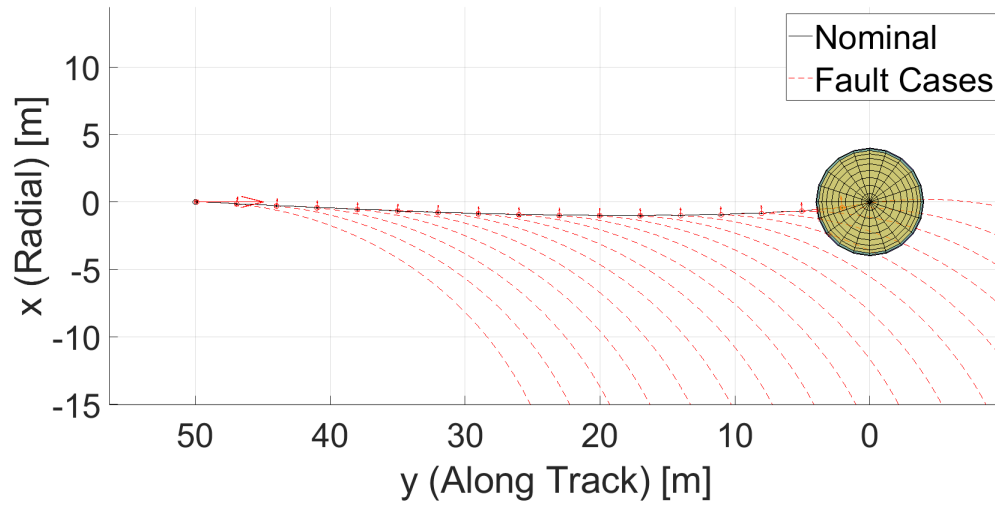
Figure 4.4. Straight-line transfer trajectory showing the propagated trajectory from post-maneuver state estimate.
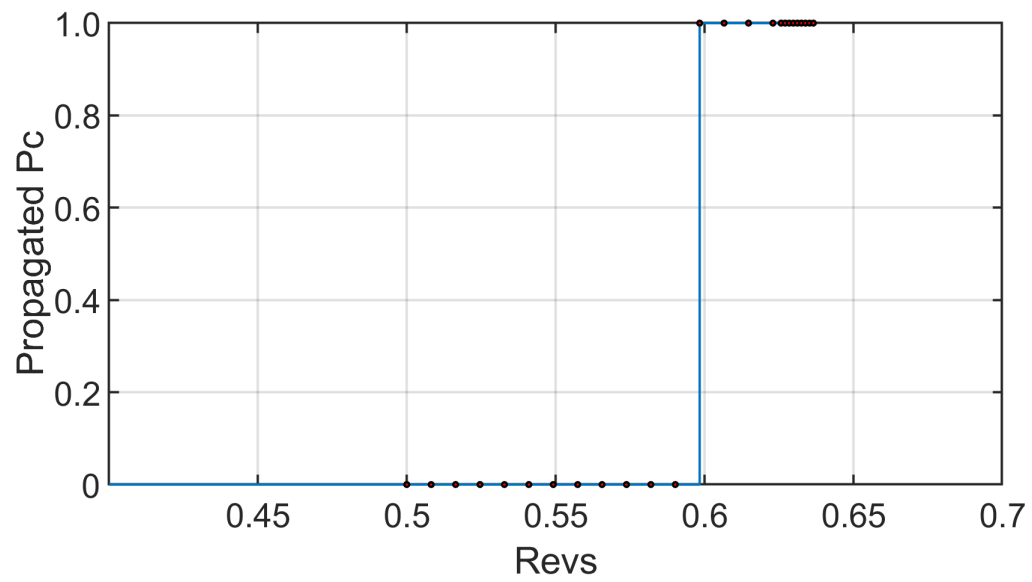

Figure 4.5. Straight-line transfer propagated collision probability

4.2.3 Two-Phase Transfer

The third case that was evaluated consisted of four initial radial impulse transfer hops followed by a straight-line approach along the V-bar. This trajectory can be seen for both the simplified mode and the high-fidelity mode in Figure 4.6. Figure 4.7 shows that the first four radial impulse transfer hops were passively safe, and return to the initial location of the impulse.

This feature of the tangential impulse hops allows for the transfer to be attempted a second time provided the fault that prevented the subsequent maneuver can be cleared in one rev. If the fault persists, state uncertainty at the time of the fault will result in the covariance continuing to grow to account for deviations from the nominal trajectory. Given sufficient time, the collision probability could be substantial. However, as discussed in Section 3.1.3 the simulation assumed that for faults lasting more than one rev, the on-board fault protection system would be able to take sufficient action to either address the fault or actively abort to a predetermined orbit until the issue could be addressed.

Figure 4.8 shows that the propagated probability of collision jumped from zero to one at the transition point between phases due to the reduced time for the covariance to expand with the straight-line transfer approach.

Table 4.5 shows that this two-phase approach had a slightly lower total probability of collision than the entirely straight line approach.

Total Collision Probability	$0.0006 \pm .00000$
Total Impulse	78.36 mm/s
Number of impulses	7
Elapsed time	2.04 Revs (249.02 min)

Table 4.5. Two-phase transfer case study results
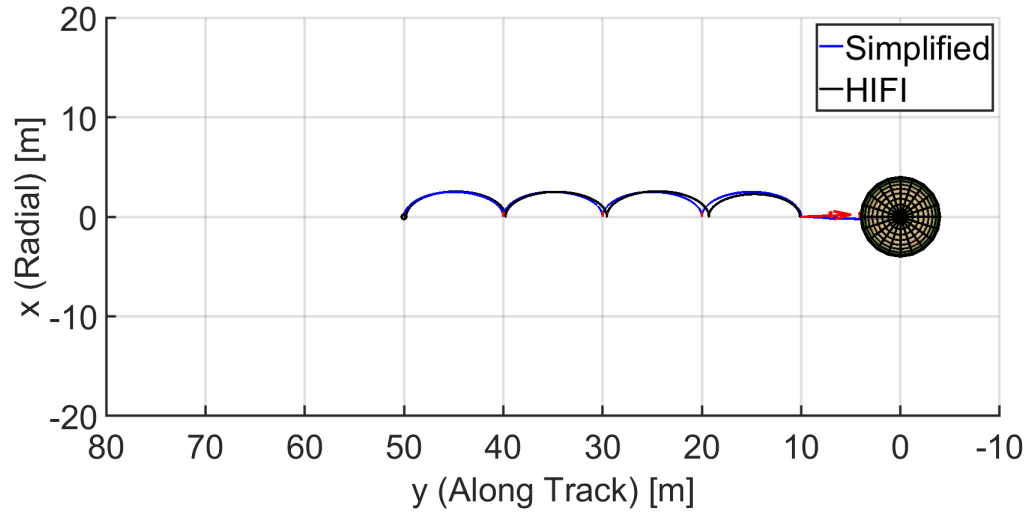
Figure 4.6. Two-phase transfer trajectory from four radial impulse transfer hops transitioned to straight-line transfer at ten meters showing simplified and HIFI models
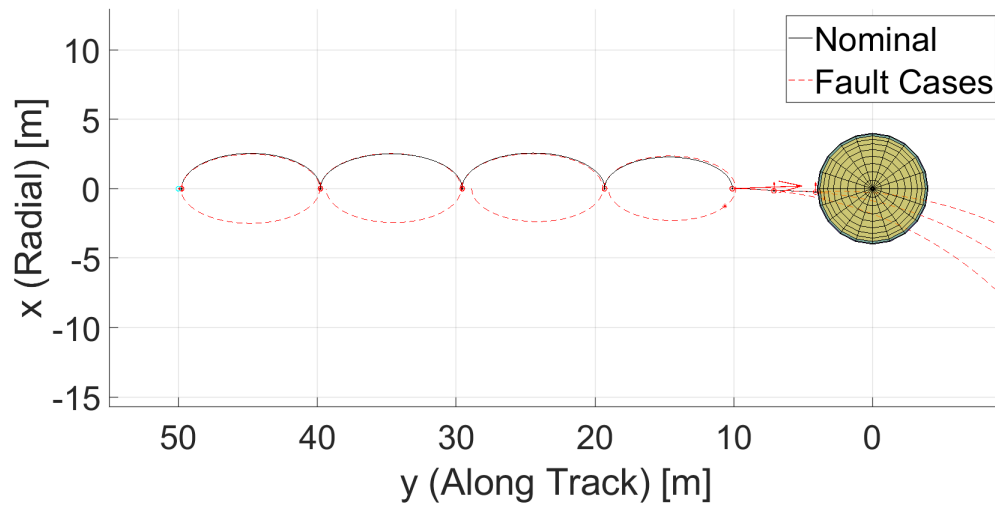

Figure 4.7. Two-phase transfer trajectory showing propagated trajectory based on post-maneuver state estimate.
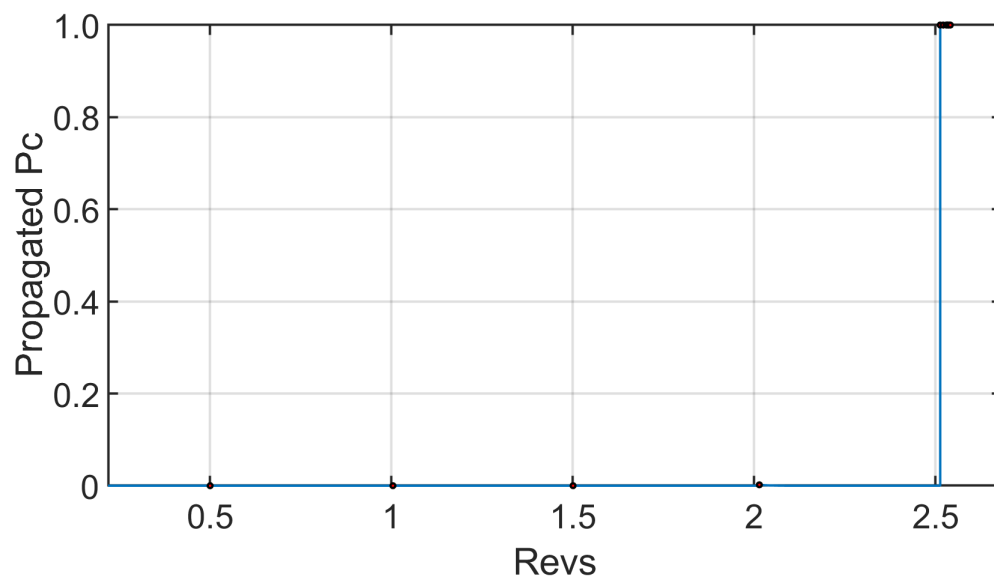
Figure 4.8. Two-phase transfer propagated collision probability

4.3 Trajectory Trade Studies

4.3.1 Radial Impulse Hops in Ballistic Transfer

Figure 4.9 shows the effect of breaking up the trajectory into smaller V-bar hops. This figure shows that when the capture occurred at the hardbody radius, smaller intercept radial impulse hops reduce total collision probability until the penultimate hop became an intercept trajectory as was the case for 13 hops to transfer 50 meters (3.846 m/hop) with a 4-meter combined hardbody radius. When the capture occurred at 1/4 the hardbody radius, a minimum collision probability of 0.013 occurred for 7 hops (7.14 m/hop). This result indicates that the primary reason the total collision probability is reduced with increasing hops is because of the larger portion of the smaller hops that is taken up by the successful capture. The slight minimum at 6 hops that occurs for the capture at the origin, however, indicates that there is some reduction in total collision probability due to introducing more time spent on a passively safe trajectory. This is likely because that a fault becomes more likely with the increased time associated with increasing the number of hops. This would indicate that the probability of having a successful rendezvous, as determined by the probability that no faults occur, also decreases with increasing hops.
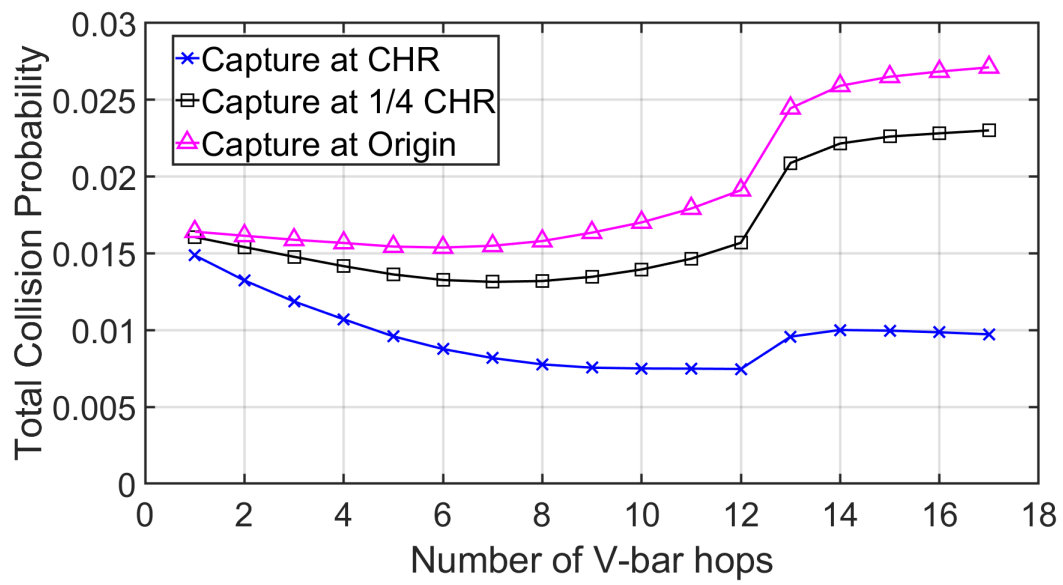
Figure 4.9. Total collision probability vs number of radial impulse hops

4.3.2 Phase Transition Location in Two-Phase Transfer

Figure 4.10 shows the effects of changing the transition point from V-bar hops to a straight-line approach. Figure 4.10 shows that there was very little change in total collision probability between a straight-line transfer ($P_T = 0.0011$) and a two-phase transfer with a transition point greater than 10 meters along the V-bar ($+\hat{y}$), but that a transition less than 1 meter from the combined hardbody radius can introduce significantly more risk. Figure 4.11 shows that refining Figure 4.10 around the transition region at 10 meters does not produce a significant minimum collision probability before the increase begins.

Figure 4.12 shows the same trade study as Figure 4.11 when additional passive safety was added by lowering the instantaneous center of motion. This additional passive safety during the first phase of the approach introduced a minimum collision probability of 0.0006 when the transition point was located between 5 and 6.5 meters. This local minimum demonstrates that there was additional risk of a collision occurring one rev after a fault occurs just prior to the transition between phases.

Figure 4.13 shows the propagated collision probability for the two-phase approach where the phase transition occurred at 6 meters. The propagated collision probability increased as the trajectory approached the end of the two-phase final radial transfer hop, counteracting any reduction in collision probability due to the slightly shorter straight-line approach phase. As expected, Figure 4.14, showing the propagated collision probability for the two-phase transfer with a center of motion of -2m, does not show this increase in propagated collision probability at the end of the final hop. Comparing the time axis of Figures 4.13 and 4.14 shows that the time for each hop is reduced when the instantaneous center of motion is lowered. This is evident both in the time that the final hop occurs (almost half a rev sooner) and in the corresponding reduction in propagated collision probability immediately following the maneuver.
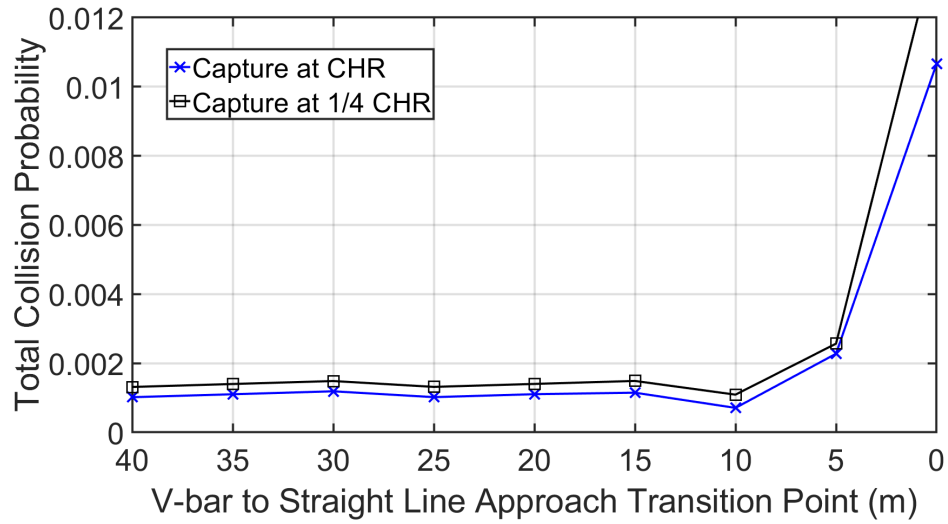
Figure 4.10. Total collision probability vs two-phase transfer phase transition point
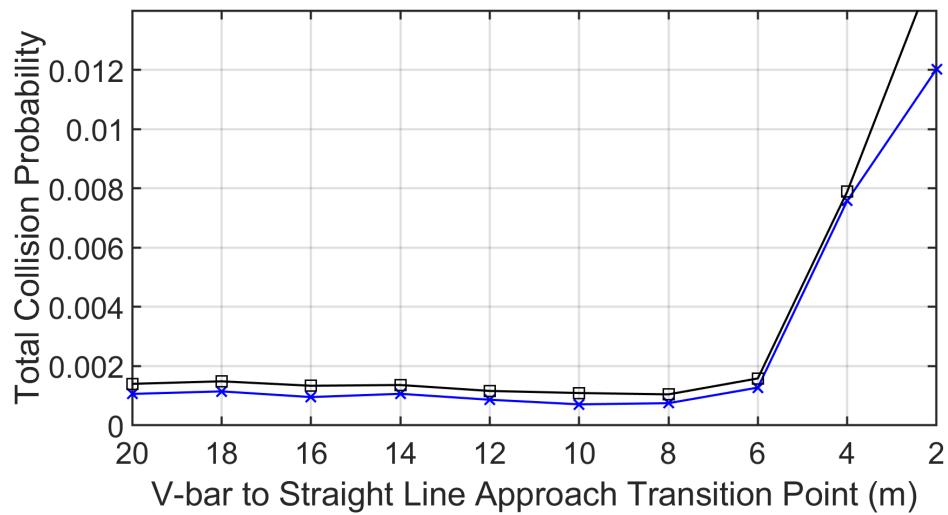
Figure 4.11. Total collision probability vs two-phase transfer phase transition point (increased resolution)
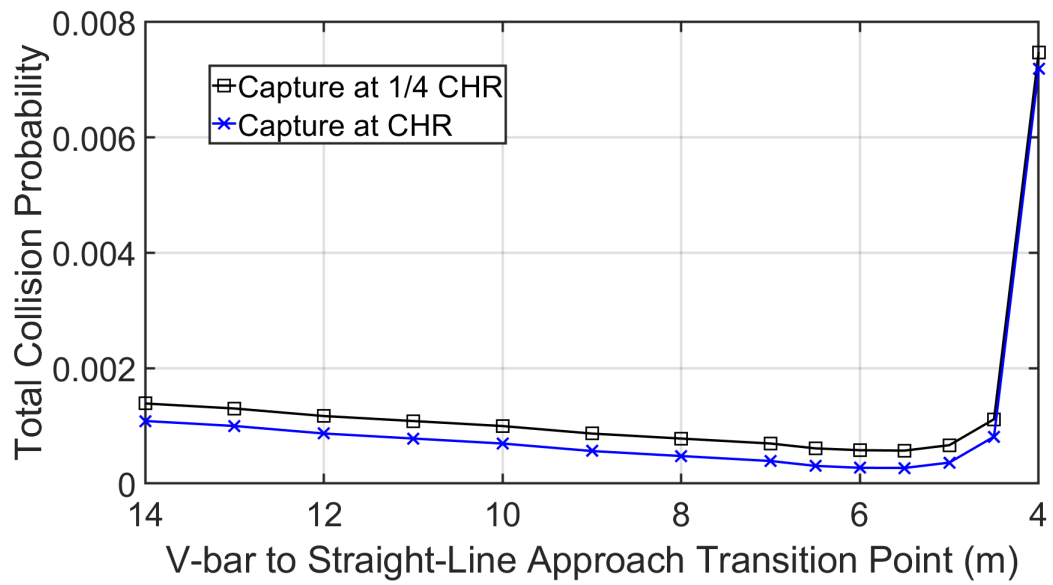
Figure 4.12. Total collision probability vs two-phase transfer phase transition point (increased resolution) for transfer hop instantaneous center of motion of -2 meters
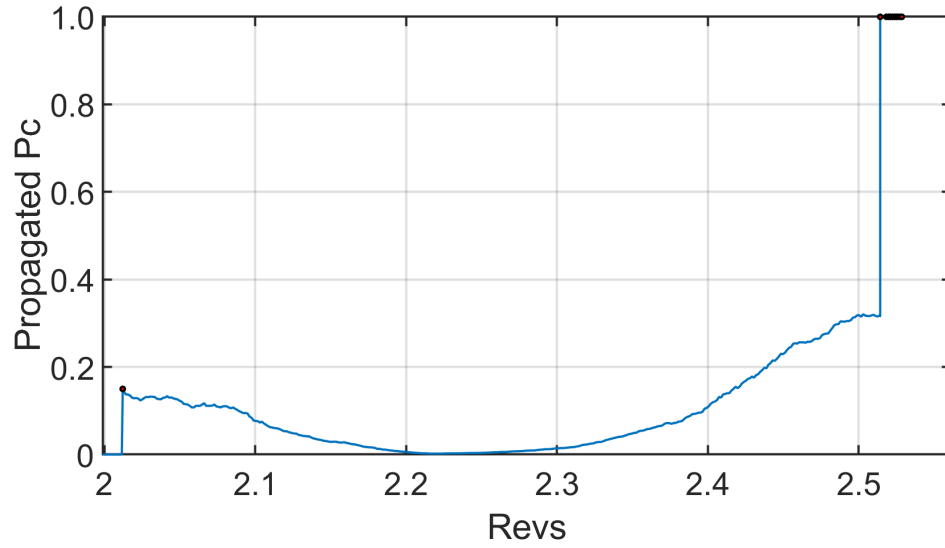
Figure 4.13. Two-phase transfer propagated collision probability with phase transition point at 6 meters showing only the final radial impulse transfer
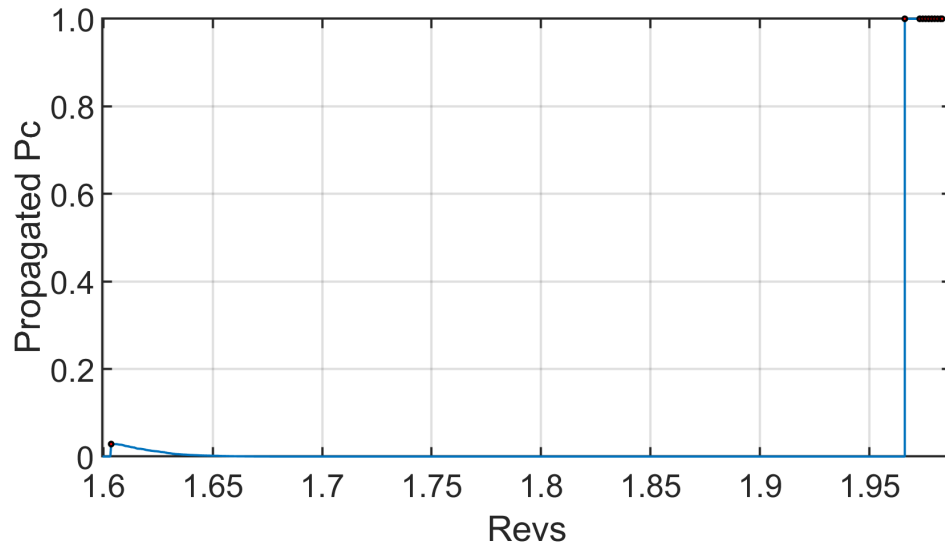
Figure 4.14. Two-phase transfer propagated collision probability with phase transition point at 6m for transfer hop instantaneous center of motion of -2 meters, showing only the final radial impulse transfer

5. CONCLUSIONS AND FUTURE WORK

Sections of this chapter have been adapted from reference [1].

As the number of commercial or routine rendezvous missions increases, so too does the need for a framework for evaluating rendezvous mission risk. The modular framework presented in this thesis allows engineers and other stakeholders to directly see the impact of trajectory design decisions on the probability that a fault during the rendezvous will result in a collision between the two spacecraft. This probability of collision is a metric which can be used to inform decisions that would previously have been made by gut instinct. As this framework developed in this thesis continues to be applied to more varied situations, teams will be able to make educated rendezvous mission design decisions without relying on intuition.

The trade studies performed for this thesis show that it is possible to provide justification for design decisions based on collision probability. The trade studies demonstrate that the biggest driver of rendezvous mission risk is the time spent on a nominal intercept trajectory. A ballistic trajectory formed by a single radial impulse takes just under half an orbit from the time of the impulse until a successful capture is achieved. Reducing the time spent on a nominal intercept trajectory by performing a straight-line transfer with multiple impulses is one way to reduce the total probability of collision. Further reductions in the total collision probability can be obtained by replacing the initial portion of the rendezvous with a passively safe transfer hop. This passively safe transfer hop can be used to replace a portion of the distance traveled on the straight-line intercept trajectory with a non-intercept trajectory. This reduction in the time spent on an intercept trajectory further reduces the total collision probability.

Future work consists of the extension of the method presented in this thesis to include additional rendezvous approaches, sensor parameters, and the effects of hard-

ware reliability. This method could be used to identify the collision probability for other rendezvous approaches, such as an R-bar approach or other control methodologies. Sensor parameters were not studied in this thesis; however the method may point towards sensors that reduce the risk of a collision during the rendezvous mission. Finally, hardware reliability and fault protection systems affect the probability of a fault. Studying these design parameters could alter some of the trends observed in this thesis. For example, substantially reducing the probability of a fault occurring may reduce some of advantages gained by adding additional time on passively safe trajectories.

This thesis directly lends itself to parameter optimization. A minimum collision probability rendezvous mission could be developed as part of future work. A multi-objective parameter optimization method could maximize the probability of no faults occurring during the rendezvous and minimize the probability that a fault would result in a collision. Additional constraints, including constraints on maximum impulse and capture conditions, could ensure the optimized rendezvous design remained feasible.

This thesis could also be extended to other dynamics regimes involving additional perturbations or other sources of error. This would likely involve the use of other dynamics and maneuver planning models. This extension would demonstrate if a design that works well for one orbit would work similarly well in a more perturbed orbit.

A Monte Carlo simulation could also be run and used to compare against the method presented in this thesis. Monte Carlo simulations are often considered the most accurate form of probability analysis and would provide a valuable comparison to the method developed in this thesis.

Additional spacecraft details or assumptions not included in this study, such as attitude and thrust capabilities, could be added to identify the transition to the unavoidable intercept zone, and to continue to increase model fidelity. These additions would allow the framework to be applied to specific rendezvous missions.

REFERENCES

[1] McClain M. Goggin and David A. Spencer. Rendezvous mission risk reduction through passive safety analysis. In *35th Space Symposium*, 2019.

[2] David Woffinden and David Geller. Navigating the road to autonomous orbital rendezvous. *Journal of Spacecraft and Rockets*, 44(4):898–909, 2007.

[3] Michael E Polites. Technology of automated rendezvous and capture in space. *Journal of Spacecraft and Rockets*, 36(2), 1999.

[4] Buzz Aldrin. Line-of-sight guidance techniques for manned orbital rendezvous, 1963.

[5] Robert C. Dempsey. *The International Space Station : operating an outpost in the new frontier*. NASA SP (Series) ; 2017-634. National Aeronautics and Space Administration, Lyndon B. Johnson Space Center, 2017.

[6] Bryan Burrough. *Dragonfly : NASA and the crisis aboard MIR*. Harper-CollinsPublishers, New York, NY, 1st ed.. edition, 1998.

[7] M. Oda. ETS-VII: Achievements, troubles, and future. In *Proceedings of the 6th International Symposium on Artificial Intelligence and Robotics and Automation in Space: ISAIRAS 2001*, Quebec, Canada, 2001.

[8] Overview of the DART Mishap Investigation Results. Technical report, NASA, 2006.

[9] Timothy Rumford. Demonstration of autonomous rendezvous technology (dart) project summary. *Proceedings of SPIE, the International Society for Optical Engineering*, spie-5088, 2003.

[10] Peter Z. Schulte, David A. Spencer, and McClain M. Goggin. Mars Sample Return Terminal Rendezvous State-Based Fault Protection. *Manuscript Submitted for Publication*, 2018.

[11] Louis S. Breger and Jonathan P. How. Safe Trajectories for Autonomous Rendezvous of Spacecraft. *Journal of Guidance, Control, and Dynamics*, 31(5):1478–1489, 2008.

[12] Diane S. Koons, Craig Schreiber, Francisco Acevedo, and Matt Sechrist. Risk mitigation approach to commercial resupply to the international space station. In *European Space Agency, (Special Publication) ESA SP*, volume 680, 2010.

[13] Mohinder S Grewal and Angus P Andrews. Applications of kalman filtering in aerospace 1960 to the present [historical perspectives]. *IEEE Control Systems*, 30(3):69–78, 2010.

[14] G. W. Hill. Researches in the lunar theory. *American Journal of Mathematics*, 1(2):129–147, 1878.

[15] D.P. Scharf, F.Y. Hadaegh, and S.R. Ploen. A survey of spacecraft formation flying guidance and control. Part II: control. In *Proceedings of the 2004 American Control Conference*, 2004.

[16] K. T. Alfriend and H. Yan. Evaluation and Comparison of Relative Motion Theories. *Journal of Guidance, Control, and Dynamics*, 28(2):254–261, 2005.

[17] Joshua Sullivan, Sebastian Grimberg, and Simone D'Amico. Comprehensive Survey and Assessment of Spacecraft Relative Motion Dynamics Models. *Journal of Guidance, Control, and Dynamics*, 40(8):1837–1859, 2017.

[18] F. De Bruijn, E. Gill, and J. How. Comparative analysis of Cartesian and curvilinear Clohessy-Wiltshire equations. *Journal of Aerospace Engineering, Sciences and Applications*, 3(2):1–15, 2011.

[19] David A. Vallado and Salvatore Alfano. Curvilinear coordinates for covariance and relative motion operations. *Advances in the Astronautical Sciences*, 142:929–946, 2011.

[20] Koji Yamanaka and Finn Ankersen. New State Transition Matrix for Relative Motion on an Arbitrary Elliptical Orbit. *Journal of Guidance, Control, and Dynamics*, 25(1):60–66, 2002.

[21] Samuel A. Schweighart and Raymond J. Sedwick. High-fidelity linearized j2 model for satellite formation flight. *Journal of Guidance, Control, and Dynamics*, 25(6):1073–1080, 2002.

[22] Gabriella Gaias, Jean Sébastien Ardaens, and Oliver Montenbruck. Model of J2 perturbed satellite relative motion with time-varying differential drag. *Celestial Mechanics and Dynamical Astronomy*, 123(4):411–433, 2015.

[23] Dong-Woo Gim and K Alfriend. State transition matrix of relative motion for the perturbed noncircular reference orbit. *Journal of Guidance, Control, and Dynamics*, 26(6):956–971, 2003.

[24] Simone D'Amico and Oliver Montenbruck. Proximity Operations of Formation-Flying Spacecraft Using an Eccentricity/Inclination Vector Separation. *Journal of Guidance, Control, and Dynamics*, 29(3):554–563, 2006.

[25] T. Alan Lovell and S. Tragesser. Guidance for Relative Motion of Low Earth Orbit Spacecraft Based on Relative Orbit Elements. In *AIAA/AAS Astrodynamics Specialist Conference, AIAA 2004-4988*, 2004.

[26] Thomas A. Lovell and David A. Spencer. Relative orbital elements formulation based upon the clohessy-wiltshire equations. *Journal of the Astronautical Sciences*, 61(4):341–366, 2014.

[27] Wigbert Fehse, Michael J. Rycroft, and Shyy Wei. *Automated Rendezvous and Docking of Spacecraft*. Cambridge Aerospace series Automated rendezvous and docking of spacecraft. Cambridge University Press, 2003.

[28] C. R. Gates. A Simplified Model of Midcourse Maneuver Execution Errors. Technical report, JPL Technical Report NO. 32-504, 1963.

[29] Vincent J. Chioma and Nathan A. Titus. Expected Maneuver and Maneuver Covariance Models. *Journal of Spacecraft and Rockets*, 45(2):409–412, 2008.

[30] Byron D. Tapley, Bob E. Schutz, and George H. Born. Fundamentals of Orbit Determination. In *Statistical Orbit Determination*, chapter 4. Elsevier Academic Press, 2004.

[31] R. E. Kalman. A New Approach to Linear Filtering and Prediction Problems. *Journal of Basic Engineering*, 82(1):35–45, 1960.

[32] Joshua Sullivan and Simone D'Amico. Nonlinear kalman filtering for improved angles-only navigation using relative orbital elements. *Journal of Guidance, Control, and Dynamics*, 40(9):2183–2200, 2017.

[33] Simon J. Julier and Jeffrey K. Uhlmann. New extension of the Kalman filter to nonlinear systems. In *Proceedings of SPIE 3068, Signal Processing, Sensor Fusion, and Target Recognition VI*, pages 182–193, 1997.

[34] J. Russell Carpenter. Non-Parametric Collision Probability for Low-Velocity Encounters. In *17th AAS/AIAA Space Flight Mechanics Meeting, AAS 07–201*, Sedona, AZ, 2007.

[35] Kenneth F. Chan. *Spacecraft collision probability.* Aerospace Press ; American Institute of Aeronautics and Astronautics, El Segundo, Calif. : Reston, Va., 2008.

[36] Michael R Phillips. Spacecraft Collision Probability Estimation for Rendezvous and Proximity Operations. Master's thesis, Utah State University, 2012.

[37] Russell P. Patera. Satellite Collision Probability for Nonlinear Relative Motion. *Journal of Guidance, Control, and Dynamics*, 26(5):728–733, 2003.

[38] David McKinley. Development of a Nonlinear Probability of Collision Tool for the Earth Observing System. In *AIAA/AAS Astrodynamics Specialist Conference, AAS/AIAA 2006-6295*, 2006.

[39] Salvatore Alfano. Addressing Nonlinear Relative Motion For Spacecraft Collision Probability. In *AIAA/AAS Astrodynamics Specialist Conference and Exhibit, AIAA 2006-6760*, Keystone, CO, 2006.

[40] A Burton, M Zielinksi, C Frueh, A Mashiku, and N Memarsadeghi. Assessing measures to reliably predict collisions in the presence of uncertainty. In *AAS/AIAA Astrodynamics Specialist Conference, AAS–18–439*, Snowbird, UT, 2018.

[41] Roger R. Bate, Donald D. Mueller, and Jerry E. White. Perturbations. In *Fundamentals of Astrodynamics*, chapter 9. Dover, New York, 1971.

[42] W. H. Clohessy and R. S. Wiltshire. Terminal Guidance System for Satellite Rendezvous. *Journal of Aerospace Sciences*, 27(9):653–658, 1960.

[43] Alonzo Kelley. A 3D State Space Formulation of a Navigation Kalman Filter for Autonomous Vehicles. Technical report, Robotics Institute, Carnegie Mellon University, 1994.

[44] Eric A. Wan and Rudolph Van Der Merwe. The unscented kalman filter for nonlinear estimation. In *Proceedings of the IEEE 2000 Adaptive Systems for Signal Processing, Communications, and Control Symposium (Cat. No.00EX373)*, pages 153–158. IEEE, 2000.

[45] Maria Isabel Ribeiro. Gaussian probability density functions: Properties and error characterization. *Institute for Systems and Robotics, Lisboa, Portugal*, 2004.

[46] Edwin B. Wilson and Margaret M. Hilferty. The distribution of chi-square. *Proceedings of the National Academy of Sciences of the United States of America*, 17(12):684–688, 1931.

[47] Christian Walck. Hand-book on statistical distributions for experimentalists. Technical report, Particle Physics Group, Fysikum, University of Stockholm, 1996.

A. RENDEZVOUS MISSION SURVEY

Table A.1.: Rendezvous mission survey

Program/ project	Organization	Time Period	Class	Operability	Chief Co-operation	Behavior
Dream Chaser	Sierra Nevada	2020+	Large	Autonomous	Cooperative, Controlled	Docking
MEV	Orbital ATK	2019+	NA	Ground-in-the-loop	Non-Cooperative, Controlled	Docking
CADRE	EPFL	2019+	Nano	Autonomous	Cooperative, Uncon-trolled	Rendezvous
CPOD	Tyvak	2019+	Nano	Ground-in-the-loop	Cooperative, Controlled	Docking
OCSD	The Aerospace Corpora-tion	2017	Nano	NA	Cooperative, Controlled	Rendezvous
Tianzhou	CNSA	2017	Large	Autonomous	Cooperative, Controlled	Docking
LoneStar Pro-gram	Texas A&M	2016	Nano	Autonomous	Cooperative Controlled	Docking

Table A.1.: *continued*

Program/ project	Organization	Time Period	Class	Operability	Chief Co-operation	Behavior
Banxing-2	CNSA/SAST	2016	Nano	Autonomous	Cooperative, Controlled	Rendezvous
ZDPS-2	CNSA	2015	Nano	Ground-in-the-loop?	Cooperative, Controlled	Formation Flying/Rendezvous
GSSAP	USAF	2014	Medium	Ground-in-the-loop	Non-Cooperative, Controlled	Rendezvous
ANGELS	AFRL	2014	Micro	Ground-in-the-loop	Cooperative, Uncontrolled	Rendezvous
Cygnus	Orbital ATK	2014	Large	Pilot-in-the-loop	Cooperative, Controlled	Docking
Dragon	SpaceX	2012	Large	Pilot-in-the-loop	Cooperative, Controlled	Rendezvous
PRISMA	ESA	2010	Mini	Ground-in-the-loop	Cooperative, Controlled	Rendezvous
HTV	JAXA	2009	Large	Pilot-in-the-loop	Cooperative, Controlled	Rendezvous
ATV	ESA	2008	Large	Autonomous	Cooperative, Controlled	Docking
Banxing-1	CNSA/CASC	2008	Nano	Autonomous	Cooperative, Controlled	Rendezvous

Table A.1.: *continued*

Program/ project	Organization	Time Period	Class	Operability	Chief Co-operation	Behavior
Orbital Express	DARPA	2007	Medium	Ground-in-the-loop	Cooperative, Controlled	Docking
SPHERES	MIT	2006	Nano	Autonomous	Cooperative, Controlled	Docking
XSS-11	AFRL	2005	Micro	Ground-in-the-loop	Rendezvous	
DART	NASA	2005	Mini	Autonomous	Cooperative, Controlled	Rendezvous
XSS-10	AFRL	2003	Micro	Ground-in-the-loop	Non-Cooperative, Uncon-trolled	Rendezvous
Shenzhou	CNSA	1999	Manned	Pilot-in-the-loop	Cooperative, Controlled	Docking
AERCam Sprint	NASA	1997	Nano	Piloted	Non-Cooperative, Uncon-trolled	Docking
ETS-VII	NASDA	1997	Large	Ground-in-the-loop	Cooperative, Controlled	Docking
KIKU-7	JAXA	1997	Large			
TAOS	AFRL	1994	Mini	Ground-in-the-loop	Cooperative, Controlled	Rendezvous

Table A.1.: *continued*

Program/ project	Organization	Time Period	Class	Operability	Chief Co-operation	Behavior
STS	NASA	1981	Manned	Piloted	Cooperative, Controlled	Docking
Soyuz	USSR	1967	Manned	Pilot-in-the-loop	Cooperative, Controlled	Docking
Apollo	NASA	1966	Manned	Piloted	Cooperative, Controlled	Docking
Gemini	NASA	1962	Manned	Piloted	Cooperative, Controlled	Rendezvous

B. METHOD OF APPROXIMATE DISTRIBUTIONS

The probability of interest for an instantaneous collision probability calculation is the probability that the true position $\bar{\rho}$, modeled as a set of three independent Gaussian random variable of mean $\tilde{\rho}_j$ (renamed $\tilde{b}$ in the following derivation) and covariance $\mathbf{C}$ lies within the combined hardbody volume of radius R_H. That is, the probability that:

$$P = P\left[r^2 \leq R_H^2\right] \tag{B.1}$$

$$P(||\bar{\rho}|| < R_H) = P(\sum_{j=1}^{k} \rho_j \leq R_H) \tag{B.2}$$

Let Ψ^2 be defined as

$$\Psi^2 = \sum_{j=1}^{n} \rho_j \tag{B.3}$$

Let b_j denote the elements of the estimated state, and σ_j denote the diagonal entries of the covariance matrix. Equation B.3 can be re-written as:

$$\Psi^2 = \sum_{j=1}^{k} \sigma_j^2 (\frac{\rho_j - b_j}{\sigma_j} + \frac{b_j}{\sigma_j})^2 \tag{B.4}$$

$$= \sum_{j=1}^{k} v_j(q_j + a_j)^2 \tag{B.5}$$

where

$$q_j = (\rho_j - b_j)/\sigma_j \tag{B.6}$$

$$a_j = b_j/\sigma_j \tag{B.7}$$

$$v_j = \sigma_j^2 \tag{B.8}$$

The probability of collision can now be determined as

$$P = P\left[r^2 \leq R_H^2\right] = P\left[\Psi^2 \leq R_H^2\right] \tag{B.9}$$

The characteristic function of a random variable with probability density function $f(x)$ takes the form similar to the Fourier transform [47]:

$$\phi(t) = E[e^{ixt}] \tag{B.10}$$

$$= \int_{-\infty}^{\infty} e^{ixt} f(x) dx \tag{B.11}$$

This can be related to the moments of the distribution through

$$\phi_x(t) = \sum_{n=1}^{\infty} (it)^n E[x^n]/n! \tag{B.12}$$

$$= \sum_{n=1}^{\infty} (it)^n \mu'_n/n! \tag{B.13}$$

where $i^2 = -1$. The expected value for a single expansion term (μ'_r) can be found as the rth derivative of the characteristic function evaluated at t=0.

$$\mu'_r = \frac{1}{i^r} \left(\frac{d}{dt}\right)^r \phi(t)\Big|_{t=0} \tag{B.14}$$

The Characteristic function $(\phi(t))$ for a noncentral chi-square distribution with non-zero mean and non-unit standard deviation is given by:

$$\phi(t) = \prod_{j=1}^{n} \phi_j(t) \tag{B.15}$$

$$= \prod_{j=1}^{n} (1 - 2it\sigma_j^2)^{(1/2)} \exp\left[\sum_{j=1}^{n} (it\sigma_j^2 a_j^2)/(1 - 2it\sigma_j^2)\right] \tag{B.16}$$

The first three moments about the mean for $\phi_j(t)$ are given by:

$$\mu = \mu'_1 \tag{B.17}$$

$$\mu_2 = \mu'_2 - \mu'^2_1 \tag{B.18}$$

$$\mu_3 = \mu'_3 - 3\mu'_2\mu'_1 + 2\mu'^3_1 \tag{B.19}$$

These moments are independent when determined for independent variables, therefore, the total mean, variance, and third moments can be determined by summing the mean, variance, and third moment for each axis.

$$m \equiv \mu = \sum_{j=1}^{n} [v_j + v_j a_j^2] = \sum_{j=1}^{n} [\sigma_j^2 + b_j^2] \tag{B.20}$$

$$v \equiv \mu_2 = 2 \sum_{j=1}^{n} [v_j^2 + 2v_j^2 a_j^2] = 2 \sum_{j=1}^{n} [\sigma_j^4 + 2\sigma_j^2 b_j^2] \tag{B.21}$$

$$\mu_3 = 8 \sum_{j=1}^{n} [v_j^3 + 3v_j a_j^2] = 8 \sum_{j=1}^{n} [\sigma_j^6 + 3\sigma_j^4 b_j^2] \tag{B.22}$$

For a central chi-square distribution(χ^2), ($a_j = 0$, $\sigma_j = 1$), the characteristic equation B.16 simplifies to:

$$\phi(t) = (1 - 2it)^{(-n/2)} \tag{B.23}$$

where n is the degrees of freedom and describes the shape of the distribution. The resulting first three moments for the central chi-square distribution are determined by:

$$\mu = n \tag{B.24}$$

$$\mu_2 = 2n \tag{B.25}$$

$$\mu_2 = 8n \tag{B.26}$$

For the non-central chi-square distribution to be approximated by the central chi-square distribution, the fit should satisfy

$$\frac{\chi^2 - n'}{\sqrt{2n'}} = \frac{\Psi^2 - m}{\sqrt{v}} \tag{B.27}$$

The non-central chi-square distribution can then be approximated by a central chi-square distribution by setting the first three moments equivalent to each other such that if $E(\cdot), V(\cdot), T(\cdot)$ denote the operators for the mean, variance, and third moment about the mean according to a desired degree of freedom n':

$$E\left(\frac{\chi^2 - n'}{\sqrt{2n'}}\right) = E\left(\frac{\Psi^2 - m}{\sqrt{v}}\right) \tag{B.28}$$

$$V\left(\frac{\chi^2 - n'}{\sqrt{2n'}}\right) = V\left(\frac{\Psi^2 - m}{\sqrt{v}}\right) \tag{B.29}$$

$$T\left(\frac{\chi^2 - n'}{\sqrt{2n'}}\right) = T\left(\frac{\Psi^2 - m}{\sqrt{v}}\right) \tag{B.30}$$

$$\tag{B.31}$$

If $E(\Psi^2) = n'$, and $v(\Psi^2) = 2n'$ to fit the central chi-square distribution, the mean and variance of the central chi-square distribution automatically align such that:

$$E(\chi^2) = n' \tag{B.32}$$

$$V(\chi^2) = 2n' \tag{B.33}$$

The third moment about the mean yields

$$T(\chi^2) = \left(\frac{2n'}{v}\right)^{3/2} \mu_3 \tag{B.34}$$

where μ_3 is the third moment about the mean of the non-central chi-square distribution. To be consistent with the definition of a central chi-square distribution, $T(\chi^2) = 8n'$, and thus the desired degree of freedom of the central chi-square distribution can be solved.

$$n' = 8v^3/\mu_3^2 \tag{B.35}$$

When $\Psi^2 = R_H^2$, let $\chi^2 = X^2$. Equation B.27 then allows the probability of collision to be determined as

$$P = P\left[r^2 \leq R_H^2\right] = P\left[\Psi^2 \leq R_H^2\right] = \left[\chi^2 \leq X^2\right] \tag{B.36}$$

Finally, the central chi-square distribution must be formulated in terms of a Gaussian distribution. The following transformation was formed in 1931 by Wilson and Hilferty [46]

$$t = \left[\left(\frac{\chi^2}{n'} \right)^{(1/3)} - \left(1 - \frac{2}{9n'} \right) \right] / \sqrt{\frac{2}{9n'}} \tag{B.37}$$

When $\chi^2 = X^2$, let $t = T$ such that

$$P = P\left[r^2 \leq R_H^2 \right] = P\left[\Psi^2 \leq R_H^2 \right] = \left[\chi^2 \leq X^2 \right] = P\left[t \leq T \right] \tag{B.38}$$

C. BODY FRAME TO LVLH FRAME ROTATION

Observations of the relative position ($\bar{z}$) comprised of a magnitude and angles α, η For a given observation of the relative position in the body frame $\bar{z} = [z_1\hat{b}_1, z_2\hat{b}_2, z_3\hat{b}_3]$, the observation vector can be converted to the LVLH frame through a rotation matrix $^R\mathbf{L}^B$, such that

$$^R\bar{z} = {}^R\mathbf{L}^{BB}\bar{z} \tag{C.1}$$

where the preceding superscript indicates the reference frame. An example of this rotation would be if the spacecraft is maintaining a fixed attitude such that the $\hat{b}_2$ body fame unit vector points along the inertial velocity, and the $\hat{b}_1$ body frame unit vector points along the orbital angular momentum vector. In this case, the only deviation from the LVLH frame is the flight path angle.

$$^R\mathbf{L}^B = \begin{Bmatrix} 1 & 0 & 0 \\ 0 & C_\gamma & S_\gamma \\ 0 & -S_\gamma & C_\gamma \end{Bmatrix} \tag{C.2}$$

D. IMPULSIVE COVARIANCE EXPANSION

When an impulsive maneuver subject to a known maneuver error is applied, the covariance can be impulsively expanded to account for the additional uncertainty.
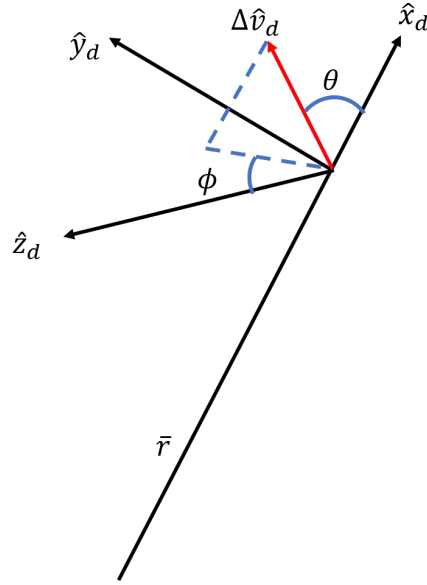

Figure D.1. Impulsive maneuver in the LVLH frame

The planned maneuver $\Delta \bar{v}$ has magnitude U and the projection of the magnitude into the $\hat{y} - \hat{z}$ plane U_{xz}

$$\Delta \bar{v} = [u_1 \hat{x}, u_2 \hat{y}, u_3 \hat{z}]^T \tag{D.1}$$

$$U = ||\Delta \bar{v}|| \tag{D.2}$$

$$U_{xz} = ||u_2, u_3|| \tag{D.3}$$

The right ascension ϕ and declination θ describe the direction of the impulse.

$$\theta = \cos^{-1}\left(u_1/||\Delta \bar{v}||\right) \tag{D.4}$$

$$\phi = \cos^{-1}(u_3/U_{xz}) \tag{D.5}$$

The rotation matrix to a frame where the planned impulse is along the $\hat{V}_x$ direction can then be formed:

$$^V\mathbf{L}^R = \begin{bmatrix} \cos(\theta) & \sin(\theta)\sin(\phi) & \cos(\phi)\sin(\theta) \\ 0 & \cos(\phi) & -\sin(\phi) \\ -\sin(\theta) & \cos(\theta)sin(\phi) & \cos(\theta)\cos(\phi) \end{bmatrix} \tag{D.6}$$

The rotation to the impulse frame is required because errors are given in terms of magnitude error applied along the planned impulse vector, and pointing errors applied in the plane perpendicular to the planned impulse vector. The impulse vector in the impulse frame then contains the entire magnitude of the planned impulse in the $\hat{v}_x$ direction.

$$\Delta\bar{v}^V = {}^V\mathbf{L}^R * \Delta\bar{v} = [U, 0, 0]^T \tag{D.7}$$

Let $\Delta\bar{v}_a$ denote the actual burn such that

$$\Delta\bar{v}_a = \Delta\bar{v} + \bar{e} \tag{D.8}$$

where $\bar{e}$ is the maneuver error vector. The expected value of the actual maneuver is then

$$E[\Delta\bar{v}_a] = \Delta\bar{v} + E[\bar{e}] \tag{D.9}$$

because the expected value of the desired burn without maneuver error is the desired burn.

The maneuver error $\bar{e}$ is comprised of both the magnitude and pointing errors $\bar{e} = \bar{e}_M + \bar{e}_P$. If M, θ, ϕ denote independent normal Gaussian random variables corresponding to the magnitude and pointing errors, then

$$\begin{bmatrix} e_x \\ e_y \\ e_z \end{bmatrix} = \begin{bmatrix} (U + M)\cos(\theta) - U \\ (U + M)\sin(\theta)\cos(\phi) \\ (U + M)\sin(\theta)sin(\phi) \end{bmatrix} \tag{D.10}$$

Because the random variables are Gaussian, their probability density functions take the form:

$$P_M(M) = \frac{1}{\sqrt{2\pi\sigma_M^2}}\exp(-M^2/(2\sigma_M^2)) \tag{D.11}$$

$$P_\theta(\theta) = \frac{1}{\sqrt{2\pi\sigma_\theta^2}}\exp(-\theta^2/(2\sigma_\theta^2)) \tag{D.12}$$

$$P_\phi(\phi) = 1/\pi, \ 0 \le \phi \le \pi, \ P_\phi = 0, \text{ elsewhere} \tag{D.13}$$

where σ_M and σ_θ are the standard deviation of the magnitude and off-axis pointing errors. Combining Equations D.10, D.11, and D.12, the expected value of the error in the maneuver direction e_x is determined as

$$E[e_x] = U\int_{-\infty}^{\infty}\cos(\theta)P_\theta d\theta + \int_{-\infty}^{\infty}\int_{-\infty}^{\infty}M\cos(\theta)P_M(M)P_\theta(\theta)d\theta dM - U \tag{D.14}$$

$$= U\int_{-\infty}^{\infty}\cos(\theta)P_\theta d\theta + \int_{-\infty}^{\infty}MP_M(M)dM\int_{-\infty}^{\infty}\cos(\theta)P_\theta(\theta)d\theta - U \tag{D.15}$$

Where evaluating the integral shows that

$$\int_{-\infty}^{\infty}MP_M(M)dM = 0 \tag{D.16}$$

$$\int_{-\infty}^{\infty}\cos(\theta)P_\theta(\theta)d\theta = e^{-\frac{1}{2}\sigma_\theta^2} \tag{D.17}$$

The expected value of the error in the maneuver direction is then

$$E[e_x] = Ue^{-\frac{1}{2}\sigma_\theta^2} - U \tag{D.18}$$

Similarly it can be shown as by [29] that

$$E[e_y] = 0 \tag{D.19}$$

$$E[e_z] = 0 \tag{D.20}$$

$$\tag{D.21}$$

The expected value of the executed maneuver is then

$$E[\Delta\bar{v}_a] = \begin{bmatrix} Ue^{-\frac{1}{2}\sigma_\theta^2} \\ 0 \\ 0 \end{bmatrix} \tag{D.22}$$

The difference between the actual burn and the expected burn is

$$\Delta \bar{v}_a - E[\Delta \bar{v}_a] = \begin{bmatrix} e_x + U - Ue^{-\frac{1}{2}\sigma_\theta^2} \\ e_y \\ e_z \end{bmatrix} \tag{D.23}$$

The covariance for the maneuver is described by

$$\mathbf{P} = E([\Delta \bar{v}_a - E[\Delta \bar{v}_a][\Delta \bar{v}_a - E[\Delta \bar{v}_a]^T) \tag{D.24}$$

Finding the expected value of each of the terms, it can be shown that all off-diagonal terms vanish, and because each of the errors is assumed to be independent, the diagonal terms reduce to the following.

$$A = .5 * (U^2 + \sigma_m^2)(1 + e^{-2\sigma_p^2}) - U^2 e^{-\sigma_p^2} \tag{D.25}$$

$$B = 1/4 * (U^2 + \sigma_m^2) * (1 - e^{-2\sigma_p^2}) \tag{D.26}$$

$$\mathbf{P} = \begin{Bmatrix} A & 0 & 0 \\ 0 & B & 0 \\ 0 & 0 & B \end{Bmatrix} \tag{D.27}$$

The covariance of the burn can then be rotated back into the LVLH frame and added to the state estimate covariance.

$$C_{vv} = {}^R\mathbf{L}^V \mathbf{P}^V \mathbf{L}^R \tag{D.28}$$